



Inertial settling of a sphere through an interface. Part 2. Sphere and tail dynamics

Jean-Lou Pierson, Jacques Magnaudet

► To cite this version:

Jean-Lou Pierson, Jacques Magnaudet. Inertial settling of a sphere through an interface. Part 2. Sphere and tail dynamics. *Journal of Fluid Mechanics*, 2018, vol. 835, pp. 808-851. 10.1017/jfm.2017.748 . hal-01660645

HAL Id: hal-01660645

<https://hal.science/hal-01660645>

Submitted on 11 Dec 2017

HAL is a multi-disciplinary open access archive for the deposit and dissemination of scientific research documents, whether they are published or not. The documents may come from teaching and research institutions in France or abroad, or from public or private research centers.

L'archive ouverte pluridisciplinaire **HAL**, est destinée au dépôt et à la diffusion de documents scientifiques de niveau recherche, publiés ou non, émanant des établissements d'enseignement et de recherche français ou étrangers, des laboratoires publics ou privés.



Open Archive TOULOUSE Archive Ouverte (OATAO)

OATAO is an open access repository that collects the work of Toulouse researchers and makes it freely available over the web where possible.

This is an author-deposited version published in: <http://oatao.univ-toulouse.fr/>
Eprints ID: 19285

To link to this article: DOI: 10.1017/jfm.2017.748
URL: <http://dx.doi.org/10.1017/jfm.2017.748>

<p>To cite this version: Pierson, Jean-Lou and Magnaudet, Jacques <i>Inertial settling of a sphere through an interface. Part 2. Sphere and tail dynamics.</i> (2018) Journal of Fluid Mechanics, vol. 835. pp. 808-851. ISSN 0022-1120</p>
--

Any correspondence concerning this service should be sent to the repository administrator: staff-oatao@listes-diff.inp-toulouse.fr

Inertial settling of a sphere through an interface. Part 2. Sphere and tail dynamics

Jean-Lou Pierson^{1,‡} and Jacques Magnaudet^{1,†}

¹Institut de Mécanique des Fluides de Toulouse (IMFT), Université de Toulouse, CNRS, INPT, UPS,
Toulouse, France

Selected situations in which a rigid sphere settles through a two-layer system obtained by superimposing two immiscible Newtonian fluids are studied using a combination of experiments and direct numerical simulations. By varying the viscosity of the two fluids and the sphere size and inertia, the flow conditions cover situations driven by capillary and viscous effects, in which case the sphere detaches slowly from the interface and may even rise for a period of time, as well as highly inertial cases where its motion is barely affected by the interface and essentially reacts to the change in the fluid viscosity and density. The evolutions of the sphere velocity, effective drag force and entrained volume of upper fluid are analysed. In most cases considered here, this entrained volume first takes the form of an axisymmetric tail which elongates as time proceeds until it pinches off at some point. We examine the post-pinch-off dynamics of this tail under various conditions. When the viscosity of the lower fluid is comparable or larger than that of the upper one, an end-pinch-off process initiated near the initial pinch-off position develops and propagates along the tail, gradually transforming it into a series of primary and satellite drops; the size of the former is correctly predicted by the linear stability theory. In contrast, when the lower fluid is much less viscous than the upper one, the tail recedes without pinching off again. During a certain stage of the process, the tip velocity keeps a constant value which is significantly underpredicted by the classical Taylor–Culick model. An improved theoretical prediction, shown to agree well with observations, is obtained by incorporating buoyancy effects resulting from the density difference between the two fluids. Spheres with large enough inertia settling in a low-viscosity lower fluid are found to exhibit specific tail dynamics prefiguring wake fragmentation. Indeed, an interfacial instability quickly develops near the top of the sphere, resulting in the formation of thin axisymmetric corollas surrounding the central part of the tail and propagating upwards. A simplified inviscid model considering the role of the boundary layer around the tail and including surface tension effects is found to predict correctly the characteristics of the observed instability which turns out to be governed by the Kelvin–Helmholtz mechanism.

Key words: interfacial flows (free surface), multiphase and particle-laden flows

[†] Email address for correspondence: jmagnaud@imft.fr

[‡] Present address: IFP Energies nouvelles, BP 3, 69360 Solaize, France.

1. Introduction

In the first part of this investigation (Pierson & Magnaudet (2017), hereinafter referred to as PM1), we analysed the results of a series of experiments in which a rigid sphere settles toward an initially horizontal interface separating two Newtonian fluids. Although small light enough spheres were observed to remain trapped at the interface, most of them were found to succeed in crossing it, entraining a certain amount of the upper fluid in their fall. This entrained volume of fluid was noticed to take a broad variety of shapes, depending on the sphere inertia, viscous, buoyancy and capillary effects.

When the sphere relative weight and the viscous force exerted by the lower fluid on the deformed interface are of comparable magnitude, the breakthrough process was observed to be slow, in line with available knowledge: under such conditions, the upper fluid contained in the film which forms ahead of the sphere is progressively squeezed out and the meniscus connecting this film to the undisturbed part of the interface lengthens gradually. At some point, the film may rupture due to van der Waals forces (this is the so-called film drainage configuration reviewed by Jeffreys & Davies 1971), or the meniscus may become unstable if the angle at which it matches with the film exceeds a critical value (O'Brien 1996). The sphere is released in the lower fluid after the first of these 'catastrophic' events happens; only the remaining fluid contained within the film or that enclosed within the lower part of the meniscus is entrained, eventually forming a small drop at the top of the sphere.

For larger sphere inertias, the breakthrough process was observed to be much faster, the sphere being able to cross the initial position of the interface without being much slowed down by capillary effects or buoyancy due to the fluid density contrast. Under such conditions, it remains connected to the upper fluid layer by a column (or tail) which lengthens as it settles within the lower fluid. This corresponds to the tailing configuration first described by Maru, Wasan & Kintner (1971) and later explored numerically in the creeping flow limit by Geller, Lee & Leal (1986). In PM1, the geometry of this column was found to strongly depend not only on the density and viscosity contrasts between the two fluids but also on the relative magnitude of inertia and viscous effects experienced by the sphere during its descent in the upper layer. This is not unlikely since their ratio determines the stability of the sphere wake, hence the possible breakdown of the flow axisymmetry past the sphere before it reaches the interface. Beyond some critical value of this ratio, the entrained column exhibits a fully three-dimensional geometry which strongly evokes that of vortices shed past axisymmetric bluff bodies translating in a homogeneous fluid, especially hairpin-like structures (see figure 4 in PM1). In contrast, when the aforementioned ratio stays below the critical value (although inertial effects are generally dominant), the column remains axisymmetric, except when a three-dimensional instability is able to develop at its surface. The latter situation was found to occur only with spheres of very high inertia sinking in a low-viscosity fluid, yielding a fragmentation process generating a large number of droplets. Leaving this situation apart, the axisymmetric column was observed to stretch until pinching off either close to the sphere or in the vicinity of the initial interface, depending on the competition between several processes.

Although the post-pinch-off dynamics of the column has little influence on the late stages of the sphere motion, it is worth studying in itself. Indeed, until it pinches off, the column may be seen as a fluid ligament continuously stretched between the initial interface and the sphere. Therefore one can expect its post-pinch-off dynamics to share strong similarities with the relaxation of initially extended drops and cylindrical liquid threads. The generic behaviours of such fluid objects were

observed and analysed in detail by Stone, Bentley & Leal (1986) and Stone & Leal (1989) (see also Stone (1994) and Eggers & Villermaux (2008) for reviews). In these seminal investigations, it was established that when such a pre-extended thread is embedded in a more viscous fluid, a so-called ‘end-pinching’ capillary instability develops in the neck region located close to its extremities, eventually leading to pinch-off, hence to the generation of drops at both ends. In contrast, no end-pinching instability was found to take place in the opposite limit where the thread is much more viscous than the surrounding fluid, the shrinking of the neck then being slowed down by the inner resistance of the thread, which makes the tips capable of receding fast enough to prevent pinch-off. Existence of a non-zero viscosity in the outer fluid was also shown to modify dramatically the nature of the self-similar evolution of the near-pinch-off thread geometry: while the radius-to-length aspect ratio tends to zero when the surrounding fluid is dynamically passive (Eggers 1993; Papageorgiou 1995), inertia plays ultimately no role when both fluids are viscous, yielding $O(1)$ near-pinch-off aspect ratios (Cohen *et al.* 1998; Lister & Stone 1998). The recent book by Eggers & Fontelos (2015) provides an up-to-date overview of fundamental aspects related to the near- and post-pinch-off dynamics.

Considering the various observations summarized above, many questions emerge, among which some of the most significant are as follows.

- (i) What kind of sphere dynamics may be expected when the sphere inertia is barely sufficient to allow it to cross the interface, making the breakthrough process controlled by capillary, buoyancy and viscous forces? How much of the upper fluid can the sphere entrain under such conditions?
- (ii) For given sphere properties (i.e. radius and density), how do the kinematic and dynamic characteristics of the sphere motion (e.g. its velocity and the drag force acting on it) vary with the viscosity and density contrasts of the two fluids in the tailing regime? How much are these characteristics influenced by the amount of entrained fluid and tail geometry?
- (iii) Which mechanisms govern the tail geometry?
- (iv) Up to which point is the post-pinch-off behaviour of the tail similar to that of a cylindrical liquid thread? Does the asymmetry in the geometry and boundary conditions at the column extremities result in some structural differences? Do buoyancy effects resulting from the density contrast between the two fluids have any influence on this behaviour?
- (v) Which types of instability can develop at the interface between the tail and the lower fluid? Under which conditions?

These are the main questions we wish to address in the present work. To make some progress on these various aspects, we jointly use experimental and computational approaches, as they nicely complement each other. For instance the hydrodynamic force acting on the sphere is much more easily obtained in computations, owing to the variety of physical effects contributing to it. Similarly, due to differences in the optical indices of the two fluids, the vorticity distribution in both fluids around the fluid–fluid interface is difficult to determine in experiments. Conversely, some small-scale phenomena, such as the late stages of film drainage and pinch-off events, may not be properly captured in computations, owing to limitations in the spatial resolution and to the approximate representation of capillary and viscous forces (Bonhomme *et al.* 2012). This may not be a serious issue, except if these small-scale features have a direct impact on the next stages of the overall dynamics. Experiments remain the ultimate ‘justice of the peace’ to appreciate this influence. In what follows,

we restrict ourselves to axisymmetric geometries which contain the essence of most phenomena related to the viscosity contrast and to buoyancy and capillary effects and allow accurate computational solutions to be obtained at a reasonable cost. Hence, situations in which the tail exhibits a non-axisymmetric geometry, reminiscent of the structure of transitional wakes past axisymmetric bluff bodies, are not considered.

The experimental protocol and measurement techniques were described in PM1 and this description will not be repeated here. Physical properties of the various fluids and spheres were also detailed in PM1. For the sake of self-consistency, let us simply recall that the two-layer fluid systems involve a layer of silicone oil on top of a bath made either of distilled water or of a glycerine–water mixture with a viscosity 88 times that of water. Three different silicone oils, hereinafter referred to as V5, V50 and V500, respectively, with viscosities 4.8, 52 and 520 times larger than that of water, respectively, are employed and all fluid pairs have interfacial tensions close to 0.03 Nm^{-1} .

Computations are performed by solving the full Navier–Stokes equations using a combination of the volume of fluid approach to track the interface evolution and the immersed boundary technique to take into account the presence of the sphere and determine the evolution of its position. The characteristics of this approach and those of the grid geometry are described in the next section; technical details regarding the immersed boundary technique and its validation are provided in appendix A. The rest of the paper deals with the analysis of the experimental and computational results obtained in three different groups of configurations. Section 3 considers two situations in which capillary and viscous effects play a leading role, making the breakthrough process dominated by the meniscus dynamics; when this process is very slow, the meniscus evolution is compared with that predicted by the Young–Laplace equation whose numerical resolution is outlined in appendix B. Sections 4 and 5 deal with situations in which the sphere acquires a sufficient energy in the upper fluid to easily cross the interface. In the configurations considered in §4, the viscosities of the two fluids are close, whereas the lower fluid is much less viscous than the upper one in the situations examined in §5. These differences in the viscosity contrast, together with those in the solid-to-fluid density contrast, yield strikingly different dynamics of the entrained column, both at short time, when it is still directly connected to the sphere, and at longer time, after its primary pinch-off. Several aspects of this dynamics are compared with existing theories in both sections. To better understand the origin of some behaviours described in §5, theoretical models are developed in appendices C and D and their predictions are compared with observations. Section 6 summarizes the main findings of this investigation and concludes with some prospects.

2. Computational approach

2.1. Governing equations

The sphere and the two immiscible fluids form a three-phase system. The evolution of this system is described within the framework of a one-fluid approach coupled with an immersed boundary method (IBM). To this end, the local fluid medium is considered as a mixture of the two Newtonian pure fluids. It may be characterized by the local volume fraction C of the upper fluid and by density and viscosity fields which depend only on C and on the intrinsic physical properties of each pure fluid. The volume fraction C obeys the hyperbolic transport equation

$$\frac{\partial C}{\partial t} + (\mathbf{U} \cdot \nabla)C = 0, \quad (2.1)$$

and the local density and viscosity of the mixture are respectively given by

$$\rho = C\rho_1 + (1 - C)\rho_2, \quad \mu = C\mu_1 + (1 - C)\mu_2, \quad (2.2a,b)$$

where indices 1 and 2 refer to the upper and lower fluids, respectively.

The flow is assumed to be incompressible and is characterized by a single velocity field \mathbf{U} and a pressure field P throughout the mixture. The governing equations, applied throughout the fluid and solid domains, are given by

$$\nabla \cdot \mathbf{U} = 0, \quad (2.3)$$

$$\rho \left\{ \frac{\partial \mathbf{U}}{\partial t} + (\mathbf{U} \cdot \nabla) \mathbf{U} \right\} = \rho \mathbf{g} - \nabla P + \nabla \cdot \{ \mu (\nabla \mathbf{U} + {}^T \nabla \mathbf{U}) \} + \mathbf{F}_\gamma + \mathbf{F}_{IBM}, \quad (2.4)$$

where \mathbf{F}_γ is the capillary force per unit volume, \mathbf{F}_{IBM} is an additional force density introduced to take into account the presence of the sphere in the way described below and \mathbf{g} denotes gravity. The capillary force is computed using the continuum surface force model designed by Brackbill, Kothe & Zemach (1992), namely

$$\mathbf{F}_\gamma = -\gamma \nabla \cdot \left\{ \frac{\nabla C}{\|\nabla C\|} \right\} \nabla C, \quad (2.5)$$

where γ is the interfacial tension which we assume to be uniform.

The IBM approach (Mittal & Iaccarino 2005; Prosperetti & Tryggvason 2007) employed to account for the presence of the moving sphere is of the body-force type (Yuki, Takeuchi & Kajishima 2007). That is, the force density \mathbf{F}_{IBM} is chosen in the form

$$\mathbf{F}_{IBM} = \alpha \rho \frac{\mathbf{U}_D - \mathbf{U}}{\tau}, \quad (2.6)$$

where \mathbf{U}_D is the desired velocity assigned to the medium at the considered location and τ denotes a characteristic time which in computational practice coincides with the time step Δt . The volume fraction α equals 1 in the solid and 0 in the free fluid. Within the solid, \mathbf{U}_D is set to $\mathbf{V} + \boldsymbol{\Omega} \times \mathbf{r}$, where \mathbf{V} and $\boldsymbol{\Omega}$ are the translational and rotational body velocities, respectively, and \mathbf{r} is the local distance to the body centre of inertia. As τ goes to zero, any difference between the fluid and body velocities tends to generate an infinite force density at locations where $\alpha \neq 0$, thus enforcing the no-slip condition.

The sphere moves according to Newton's second law. For a rigid body of volume \mathcal{V} and density ρ_p , the corresponding overall momentum balance is given by

$$\rho_p \mathcal{V} \frac{d\mathbf{V}}{dt} = \int_{\mathcal{S}} \boldsymbol{\Sigma} \cdot \mathbf{n} dS + \rho_p \mathcal{V} \mathbf{g}, \quad (2.7)$$

where $\boldsymbol{\Sigma} = -P\mathbf{I} + \mu(\nabla \mathbf{U} + {}^T \nabla \mathbf{U})$ is the stress tensor and \mathbf{n} is the local unit normal to the body surface \mathcal{S} , \mathbf{I} denoting the unit tensor. In general the torque balance is required to determine the rotation rate $\boldsymbol{\Omega}$. However we shall only consider axisymmetric situations, so that no such rotation exists, making (2.7) sufficient to predict the sphere motion.

Finally, it is important to recall that the experimental tests reported in §2 of PM1 provide evidence that silicone oil always wets the sphere surface entirely. Hence no contact line exists, so that no contact angle model is introduced in the computational approach.

2.2. Numerical techniques and grid characteristics

Computations are carried out with the JADIM code developed in our team. This code makes use of a finite volume discretization combined with a third-order Runge–Kutta Crank–Nicolson time-advancement algorithm. Centred schemes are used to evaluate the various spatial derivatives in (2.4). Incompressibility is enforced at the end of the complete time step through a projection technique (Calmet & Magnaudet 1997). The corresponding solutions of the Navier–Stokes equations are second-order accurate in both time and space. The solution of (2.1) is based on a flux corrected transport technique split along each grid direction, as described in Bonometti & Magnaudet (2007). This algorithm provides solutions for the volume fraction C with first-order accuracy in time. No explicit interface reconstruction is carried out after the C distribution is computed, so that the interface may be regarded as ‘diffuse’ in this approach. For this reason, the interfacial layer where $0 < C < 1$ may not keep a strictly constant thickness, becoming thicker (respectively thinner) in regions where the surrounding flow tends to move apart (respectively compress) the iso- C lines. An example of this behaviour may be seen in figure 1(g–h), where the iso- C contours are almost superimposed along the bottom half of the sphere while some spreading is visible along the meniscus surface. With this ‘diffuse’ approach, no specific procedure or criterion is required to capture the breakup of a fluid thread or drop. Here, such a topological change is simply a ‘through’ with $C \approx 0$ in between two fluid regions where $C \approx 1$ or *vice versa*. As the transition from $C \approx 0$ to $C \approx 1$ is achieved within 2–3 grid cells, observing such an event typically requires the two ‘plateaus’ where $C \approx 1$ to be separated by 4–6 cells. Details about the evaluation of each term in the governing equations and implementation of the various algorithms may be found in the above two references. The performances of this code in situations approaching those on which we focus here may be appreciated in the study of Bonhomme *et al.* (2012), where the dynamics of air bubbles crossing an interface between two immiscible liquids was considered. Few computational studies have been carried out so far on approaching three-phase problems. One may mention the work by Blanchette & Shapiro (2012) who considered the settling of nearly spherical drops across a two-layer arrangement of miscible fluids with identical viscosities.

Compared to the aforementioned studies, the novelty here is that we need to account for the presence of a rigid body and its interaction with the interface. As we treat the two-phase flow on a fixed grid through the volume of fluid approach, it is natural to deal with the body using the IBM technique which does not require the grid to deform with the body motion. The initial IBM approach implemented in the JADIM code is extensively described in Bigot *et al.* (2014). In this approach, equation (2.7) is solved using the technique proposed by Uhlmann (2005), i.e. the surface integral $\int_S \boldsymbol{\Sigma} \cdot \mathbf{n} dS$, whose evaluation is complex, is replaced by $\rho \mathcal{V}(dV/dt - \mathbf{g}) - \int_V \mathbf{F}_{IBM} dV$ which is much simpler to compute. Nevertheless, preliminary tests revealed that several improvements beyond the implementation described by Bigot *et al.* (2014) were desirable. A detailed presentation of these changes may be found in Pierson (2015); we summarize them in appendix A.

The axisymmetric computations whose results are discussed below were performed in a cylindrical domain with a minimum radius of $12R$ (R is the sphere radius) and a length which depends on the case under consideration, especially on the time period over which we wish to observe the dynamics of the tail towed by the sphere; this length ranges typically from $18R$ to $30R$. The interface is usually located initially $12R$ from the top of the domain. The grid is uniform in the vertical direction, z , with typically 50 cells per sphere radius. In the radial direction, r , 200 cells are

generally distributed uniformly in the central region, $0 < r \leq 4R$, so as to properly describe the boundary layer and the film that surround the sphere over a wide range of conditions; this grid density (as well as that in the z direction) is doubled in the most inertial cases for which small-scale phenomena are expected, as well as in situations where film drainage is expected to play an important role. In the outer region, $r > 4R$, the grid is non-uniform, with cells distributed following an arithmetic law. In appendix A, numerical predictions are compared with experimental data describing the settling of a sphere in a homogeneous fluid up to a Reynolds number $Re_T \approx 20$ (based on the sphere radius and terminal velocity). Very good agreement is obtained with the improved IBM technique, provided the grid comprises a minimum of 20 cells per sphere radius. We checked that the boundary layer is properly described when it contains 4–5 cells. Since its thickness is of $O(RRe_T^{-1/2})$, we are confident that the selected grid distribution with 50 cells per sphere radius provides accurate predictions up to Reynolds numbers in the range $100 \lesssim Re_T \lesssim 150$, i.e. at least up to the critical Reynolds number Re_c at which the axisymmetric flow past a freely falling sphere becomes unstable, $Re_c \approx 103$, as determined by Fabre, Tchoufag & Magnaudet (2012).

3. Two cases of meniscus-driven dynamics

In the three sections to come, we analyse in detail several configurations that were considered both experimentally and computationally. They are discussed in order of increasing magnitude of inertia effects during or after the breakthrough stage, from quasi-static detachment, to the regime preceding fragmentation in which corollas form at the back of the sphere.

The discussions to come frequently involve the five dimensionless numbers which characterize the three-phase system and were defined in PM1. Taking the upper fluid (fluid 1) as reference, these are the viscosity ratio $\lambda = \mu_2/\mu_1$, the fluid and solid-to-fluid density contrasts $\zeta = \rho_2/\rho_1 - 1$ and $\zeta_p = \rho_p/\rho_1 - 1$, respectively, the interfacial Bond number $Bo = (\rho_2 - \rho_1)R^2/\gamma$ and the Archimedes number $Ar = \rho_1(\zeta_p g)^{1/2} R^{3/2}/\mu_1$. We shall also make frequent use of the Archimedes number Ar_l based on the properties of the lower fluid, which is such that $Ar_l = 1/\lambda((\zeta_p - \zeta)(1 + \zeta)/\zeta_p)^{1/2} Ar$. Consistent with these definitions, we normalize positions, volumes and forces by the sphere radius R , volume $\mathcal{V} = (4/3)\pi R^3$ and weight $\rho_p \mathcal{V} g$, respectively, time by the gravitational time scale $(R/(\zeta_p g))^{1/2}$, hence velocity and vorticity by $(\zeta_p g R)^{1/2}$ and $(\zeta_p g/R)^{1/2}$, respectively.

3.1. A quasi-static detachment situation

We first consider the early evolution of the flow past a 14 mm diameter polyacetal sphere settling in the V500/water–glycerine pair of fluids (configuration 7b in figure 3 of PM1). The associated dimensionless parameters are $Ar = 2.2$, $Bo = 3.65$, $\lambda = 0.17$, $\zeta = 0.24$ and $\zeta_p = 0.40$.

The static force analysis developed in §4 of PM1 led to the conclusion that flotation of the sphere at the interface is possible only if $\zeta_p/\zeta \leq 3/2Bo + 1/2 + 3/4(\log(4/Bo^{1/2}) - \gamma_E)$ (equation (4.4) in PM1) for Bond numbers up to $O(1)$, γ_E denoting the Euler constant. Therefore it can be concluded that, given its weight and the magnitude of the buoyancy and capillary forces, the sphere cannot float under the present conditions. However the ratio ζ_p/ζ is only slightly larger than the sum of the terms in the right-hand side of the above inequality (see figure 7 of PM1), so that the sphere is expected to detach slowly from the interface. This is indeed the case,

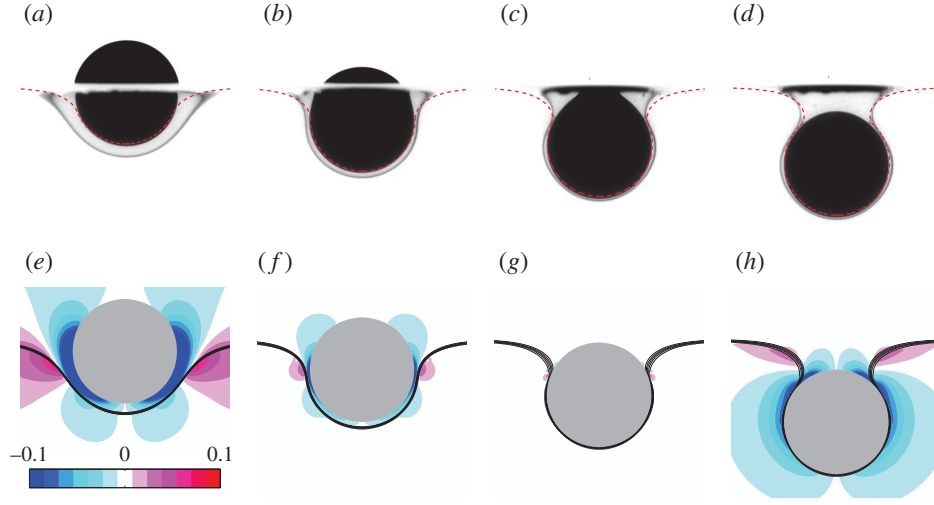


FIGURE 1. (Colour online) Four stages of the quasi-static detachment of a 14 mm diameter polyacetal sphere from a V500/water–glycerine interface. (a–d) Experimental sequence, the dashed line representing the corresponding static meniscus profile obtained by solving numerically the Young–Laplace problem (see appendix B; the film coating the spherical cap located below the meniscus is neglected in this approach). (e–h) Numerical sequence at the same instants of time, with levels of azimuthal vorticity $\omega_a = \partial u_r / \partial z - \partial u_z / \partial r$, from -0.1 to $+0.1$, according to the colour scale; the thick solid line materializing the interface is actually made of iso-contours $C = 0.1, 0.3, 0.5, 0.7, 0.9$ of the volume fraction defined in (2.1).

and we observed that it takes approximatively 30 s for the meniscus to pinch off and the sphere to start settling in the lower fluid.

Figure 1 displays four snapshots of the meniscus evolution, from the time at which the sphere is half-immersed in each fluid to that at which it stands entirely below the initial position of the interface. These four views are selected because they correspond to specific values of the angle ψ at which the film located ahead of the sphere and the meniscus match, namely $\psi = 3\pi/8, \pi/2, 5\pi/8$ and $3\pi/4$, respectively (with $\psi = 0$ at the sphere bottom). Figure 1(a–d) compares the experimental shape of the interface with the prediction provided by the numerical solution of the Young–Laplace problem (see (B 1)–(B 2) in appendix B). The agreement is very good, indicating that the system essentially undergoes a quasi-static evolution. The experimental and computational sequences show the progressive drainage of the film which first forms ahead of the sphere. As ψ increases, the change in the interface curvature in the subregion where the film and the meniscus match becomes more abrupt and locally induces a large pressure gradient within the inner (i.e. upper) fluid. The corresponding fluid acceleration results in a ‘dimple’ of the film near the equator of the sphere when ψ becomes close to $\pi/2$ (figure 1b,f), in line with the asymptotic prediction of Jones & Wilson (1978). Throughout the sequence, one may notice a region of positive vorticity in the lower fluid in the meniscus region; it originates in the negative radial velocities going with the deformation of the interface, first all along the meniscus (panel e), then in the dimple subregion (f,g) and eventually above the neck (h). This last frame corresponds to the stage at which the meniscus is close to snapping: as shown by O’Brien (1996), the Young–Laplace problem does not have a solution for

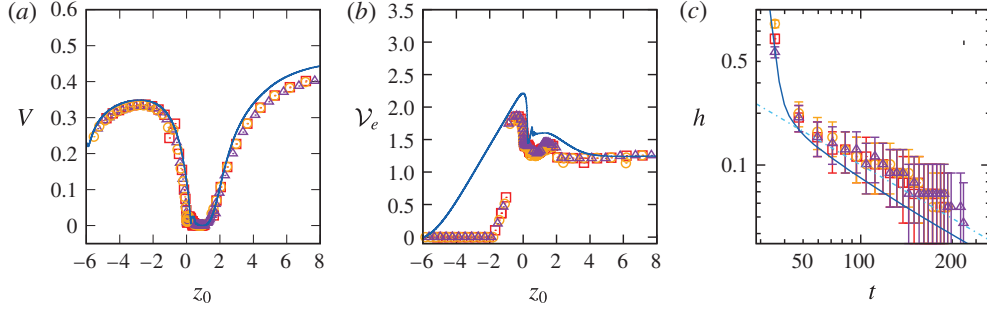


FIGURE 2. (Colour online) Evolution of three characteristics of the quasi-static breakthrough in the configuration considered in figure 1. (a) Settling velocity V as a function of the distance z_0 from the sphere centre to the initial position of the interface; (b) displaced volume \mathcal{V}_e from the initial position of the sphere ($z_0 \rightarrow -\infty$) until its current position; (c) film thickness $h(t)$ at the bottom of the sphere. Solid line: computational prediction; triangles, squares and circles refer to three different experimental tests. In (c), the dash-dotted line is a guide to the eye with a -0.65 slope; the experimental uncertainty Δh is estimated to ± 3 pixels, making $\Delta h/h$ increase as $h \rightarrow 0$.

all ψ and, in the low- Bo limit, a static equilibrium is not possible when $\psi \gtrsim 3\pi/4$. Hence somewhat later the sphere starts falling freely in the lower fluid.

Figure 2 shows how three key characteristics of this flow configuration, namely the sphere velocity V , the volume \mathcal{V}_e displaced through the lower fluid and the film thickness h ahead of the sphere, vary with the position z_0 of the sphere centre of mass (defined with respect to the initial position of the interface, with $z_0 < 0$ (respectively > 0) when the sphere stands above (respectively below) the interface). As shown in figure 2(a), after having reached its equilibrium value $V \approx 0.35$ in the upper fluid, the sphere velocity starts decreasing sharply one diameter above the interface ($z_0 \approx -2$). It falls to zero and remains negligibly small within the range $0 \leq z_0 \leq 1.5$ corresponding to figure 1(a–d). The meniscus snaps when the sphere stands at $z_0 \approx 1.5$, as will be confirmed by examining figure 2(b). Then the sphere is released in the lower fluid and accelerates progressively. Computational and experimental evolutions are in excellent agreement up to $z_0 = 2.5$. The 9% overestimate of the final settling velocity is due to a slight underestimate in the film thickness and entrained drop volume, \mathcal{V}_d : the net weight of the compound settling body being $(\rho_p - \rho_2)g\mathcal{V}(1 - \zeta/(\zeta_p - \zeta)(\mathcal{V}_d/\mathcal{V}))$, with here $\zeta/(\zeta_p - \zeta) \approx 1.54$, an underestimate of the relative entrained volume $\mathcal{V}_d/\mathcal{V}$ by 0.035 is sufficient to generate the observed overestimate in V . Assuming that the shape of the compound body is close to a sphere, this corresponds to a 1% underestimate in its equivalent radius, which is consistent with the limitation imposed by the computational grid, which in this case involves 100 cells per sphere radius.

Figure 2(b) shows how the displaced volume \mathcal{V}_e , defined as the volume comprised between the current and initial positions of the interface, i.e. $\mathcal{V}_e(t) = 2\pi \int_{z<0} C(r, z, t)r dr dz$, varies with z_0 (note that this volume includes that of the sphere, so that the normalized entrained volume of light fluid $\mathcal{V}_d/\mathcal{V}$ equals $\mathcal{V}_e - 1$). The computational prediction indicates that \mathcal{V}_e increases almost linearly from $z_0 \approx -6$ to $z_0 = 0$ ($z_0 = 0$ corresponds to figure 1a), where the displaced volume of fluid approximately equals that of the sphere. Hence the interface starts deforming well before the sphere gets close to it. This is of course the signature of the slow spatial decay of the disturbance generated by the sphere in the present $O(1)$ Reynolds number

regime. Owing to a combination of limitations inherent to optical resolution, finite field of view and post-processing procedure, this early growth of \mathcal{V}_e is not captured in experimental data, where interface deformations appear only much later, when $z_0 \approx -2$. However the two determinations further converge, providing similar peak values at $z_0 = 0$ and being in good agreement in later stages. Starting from its maximum at $z_0 = 0$, \mathcal{V}_e first decreases sharply due to film drainage. Then it increases again slightly owing to the lengthening of the meniscus, until the latter snaps at $z_0 \approx 1.5$. The upper part of the meniscus then recedes toward the initial position of the interface, making $\mathcal{V}_e - 1$ decrease towards a non-zero final value of approximately 0.2 (note the good agreement between the experimental and computational final values, although the latter is slightly smaller than the former, in line with the aforementioned underestimate). The latter is provided by the lower part of the meniscus which recedes toward the sphere, giving birth to a spherical cap drop attached to its top part and approximately limited by the cap angle $\psi_d = 3\pi/4$ at which the meniscus snapped. The way the volume of drops remaining attached to the sphere varies with the dimensionless parameters of the system was discussed in §5 of PM1. It was shown that when the viscosity ratio is large and the sphere is light, i.e. $\lambda \gg 1$ and $\zeta_p/\zeta = O(1)$, the drop volume is close to that found under static conditions in the so-called pendant drop configuration. For that problem, predictions resulting from the numerical solution of the Young–Laplace problem are available in the literature (Shoukry, Hafez & Hartland 1975; Smith & Van de Den 1985). Fitting corresponding results revealed that the drop volume varies approximately as $\mathcal{V}_e - 1 = 0.89Bo^{-1.12}$. In the present case, $Bo = 3.65$, so that this fit indicates that $\mathcal{V}_e - 1$ should be approximately 0.21, in excellent agreement with the final value observed in figure 2(b). It is interesting to notice that, in an attempt to predict the motion of small porous spheres across a sharp stratification separating two miscible fluids, Camassa *et al.* (2013) developed a model in which Stokes drag, buoyancy and the instantaneous sphere weight are in balance. They found that this model was unable to predict correctly the retention time of the sphere at the interface, unless its radius was increased so as to take into account schematically the entrainment of light fluid, thus modifying the effective buoyancy force. Yick *et al.* (2009) also examined the influence of fluid entrainment on the drag of a sphere settling in a linearly stratified fluid and showed that drag enhancement is essentially due to the entrainment of light fluid within a thin region surrounding the sphere, the size of which is determined by the fluid viscosity and the Brunt–Väisälä frequency. Here, the fluids are immiscible and entrainment of light fluid takes the form of an attached drop, which indeed decreases the net weight of the compound body by nearly 30% and slightly increases the friction drag, thus significantly delaying the release of the sphere in the lower fluid.

The evolution of the dimensionless film thickness $h(t)$ at the bottom of the sphere is shown in figure 2(c). During a first stage, h quickly decreases since the sphere is not yet slowed down by the interface. Then the film starts to be drained when $h \lesssim 0.2$, which yields a $t^{-0.65}$ decrease at later times. Experimental and computational results are in fairly good agreement throughout this two-stage evolution and both of them exhibit the above decay law (differences noticed during the drainage are most likely related to the treatment of the transition region around the sphere in the IBM technique, and the aforementioned limitation of the spatial resolution). The decay observed in figure 2(c) is somewhat faster than the well-known $t^{-1/2}$ law derived by Hartland (1969) and Jones & Wilson (1978). The most probable reason for this difference is the influence of buoyancy, which was neglected in these two studies. Indeed, Smith & Van de Ven (1984) showed that buoyancy effects due to the density

contrast between the two fluids reduce the film thickness in the region close to the symmetry axis of the system (i.e. near the bottom of the sphere), thus accelerating the drainage. Considering the present situation with $Bo = 3.7$ in which the drainage starts approximately when $h = 0.2$, their results with $\psi = \pi/3$ indicate that the time it takes for the bottom region of the film to be entirely drained (i.e. $h = 0$) is two orders of magnitude shorter than in the low Bond number limit, giving strong credit to a faster decrease of $h(t)$ due to buoyancy in the present case.

3.2. When the sphere hesitates

We now consider the motion and flow induced by a 7 mm diameter polyacetal sphere settling through a V5/water–glycerine arrangement. This situation (which corresponds to configuration 13a in PM1) is quite similar to that examined above, except that the upper fluid is a hundred times less viscous and somewhat lighter. The corresponding dimensionless parameters are $Ar = 86$, $Bo = 1.1$, $\lambda = 18.3$, $\zeta = 0.32$ and $\zeta_p = 0.48$. According to the flotation criterion mentioned above, the sphere would float at the interface if released from rest just above it (we performed this test and found that the sphere was still floating 24 h after it was released). However, under the present conditions, it reaches the interface with a significant velocity. As figure 3 shows, it turns out that the corresponding kinetic energy is sufficient to overcome capillary effects, allowing the sphere to detach from the interface (the inertial mechanisms involved in this process were discussed in § 4 of PM1). However, owing to the strong viscosity contrast, the Archimedes number in the lower fluid is only $Ar_l \approx 3.2$. Hence viscous effects are expected to play an important role in the post-detachment stage. Moreover the fluid density contrast is significant, so that the apparent weight of the sphere is reduced by one-third in the lower fluid. These two characteristics hamper its penetration in that fluid and generate a ‘rebound’ during which its velocity is positive, so that the sphere tends to come back toward the interface (figure 3d,e,k,l). A similar reversal of the motion of a sphere sedimenting in a sharp two-layer configuration with fresh water on top of salt water was reported by Abaid *et al.* (2004), who modelled the phenomenon by considering the effective buoyancy force resulting from the entrained fluid.

Comparing interface shapes in figure 3(a–d) with those of figure 1 suggests that the meniscus does not obey a quasi-static equilibrium in the present case. Indeed, the maximum ‘submergence’ (i.e. the distance from the sphere centre to the initial interface) found under quasi-static conditions in the limit $Bo \ll 1$ (see equation (4.3) in PM1) is approximately 1.2 while it is twice as large in figure 3(c). This larger submergence is made possible by the collapse of the sphere wake which provides an additional downward impulse (see the evolution of the vorticity distribution in the upper fluid in figure 3i,j). Then, when this collapse is completed, the residual kinetic energy of the sphere+fluid system is no longer sufficient to balance the large buoyancy effects resulting from the deflection of the meniscus (see § 4 in PM1), forcing the meniscus to recede in order to lower its height. This recession is accompanied by the rise of the sphere. At the same time, fluid is expelled upward from the neck of the meniscus, generating positive vorticity on both sides of the interface since the lower fluid is much more viscous and thus rises more slowly (figure 3l). Owing to volume conservation, this upward fluid motion forces the neck to shrink, making the meniscus enter an unstable state and leading inescapably to its pinch-off. The sphere may then fall in the lower fluid with a small drop of light fluid standing on its top part and still connected to the very thin film which goes on coating the rest of its surface (figure 3f,g,m,n).

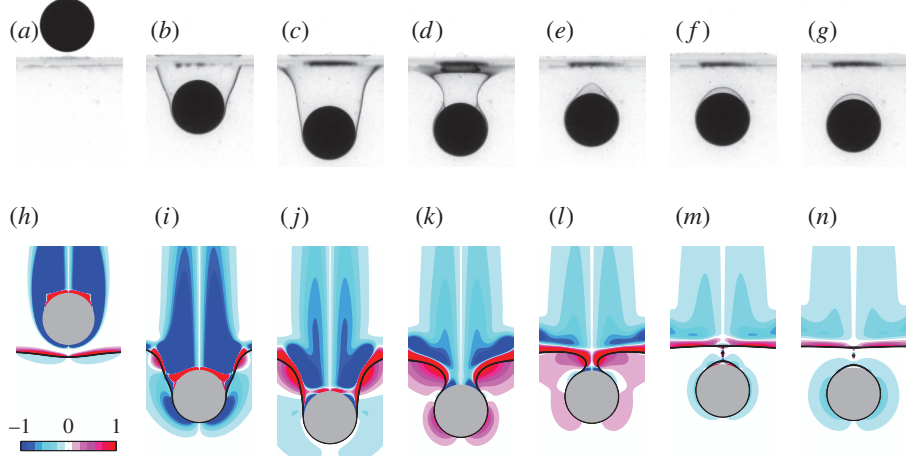


FIGURE 3. (Colour online) A 7 mm diameter polyacetal sphere settling in the V5/water-glycerine pair of fluids. (a–g) Experimental sequence; (h–n) numerical sequence at the same instants of time (see figure 1 for legend); the time interval between two panels is $\Delta t = 2.2$.

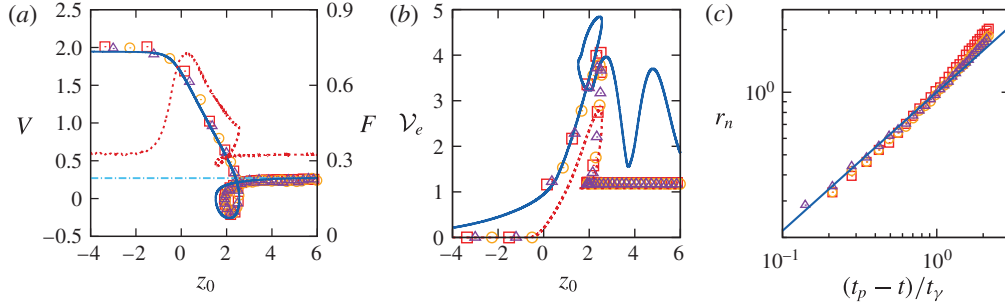


FIGURE 4. (Colour online) Evolution of four characteristics of the configuration considered in figure 3. (a) Settling velocity $V(z_0)$ and effective drag force $F(z_0)$; (b) displaced volume $V_e(z_0)$; (c) radius $r_n(t)$ of the neck. Triangles, squares and circles refer to three different experiments. In (a), the solid and dotted lines refer to the computational prediction for V and F , respectively, and the dash-dotted line corresponds to the Oseen prediction for V ; in (b) the solid and dotted lines refer to the entrained volume computed as $2\pi \int_{z < 0} C r dr dz$ and $2\pi \int_{z < -1} C r dr dz$, respectively; in (c) the solid line is the best fit of experimental data with a $2/3$ slope and t_γ stands for the capillary time scale, $t_\gamma = (\rho R^3 / \gamma)^{1/2}$.

Figure 4(a) reveals that V starts decreasing only when $z_0 \approx -1$, i.e. when the sphere almost touches the interface. Somewhat earlier, the dimensionless vertical force, $F = \mathbf{F} \cdot \mathbf{e}_z$, defined from (2.7) as $\rho_p g V F = \mathbf{e}_z \cdot \int_S \boldsymbol{\Sigma} \cdot \mathbf{n} dS - \rho_1 V g$ (\mathbf{e}_z being the unit vector in the vertical direction), starts to increase sharply (this definition implies that $F \rightarrow \zeta_p / (1 + \zeta_p)$ when $z_0 \rightarrow \pm\infty$ if the sphere moves with constant velocity). This is the consequence of the large viscosity of the lower fluid and of the significant fluid density contrast: both make the interface hard to deform, so that

the present situation resembles that of a sphere sedimenting toward a horizontal rigid wall. The force more than doubles from $z_0 = -2$ to $z_0 = 0$. A splitting of this force at $z_0 = 0$ (not shown in the figure) indicates that the capillary component and the extra buoyancy components resulting from the fluid density contrast and the deflection of the meniscus (i.e. the contributions associated with volumes \mathcal{V}_{cyl} and \mathcal{V}_{spc} in (4.1) of PM1) contribute to F by 40 % and 20 %, respectively, the last 40 % being provided by the dynamic component, essentially through the quasi-steady drag. The velocity goes on decreasing linearly almost up to the maximum submergence, $z_0 \approx 2.5$, where V falls abruptly to zero. The force experienced by the sphere decreases regularly from $z_0 = 0$ to $z_0 = 2.5$, where the total static contribution (not shown) made of the capillary force plus the various buoyancy contributions is found to be about $1.85F$, owing to the large buoyancy force induced by the light fluid enclosed in the meniscus. This splitting is interesting because it reveals that dynamic effects related to the sphere deceleration provide a large negative (i.e. downward) contribution, about $-0.85F$, so that the resulting hydrodynamic force is only F . After the sphere has reached the position $z_0 = 2.5$, the sign of its velocity reverses and it rises up to $z_0 \approx 1.5$, where V vanishes again. This rise is associated with a decrease in F , since the drag resulting from this upward motion is directed downward. It may be noticed that a loop, qualitatively similar to that observed here, was also observed in several of the aforementioned experiments by Abaid *et al.* (2004). As the fluids were miscible in that case, this similarity indicates that buoyancy alone is capable of generating this intriguing behaviour. When the sphere is eventually released in the lower fluid, V recovers its initial sign and quickly reaches its final value, V_T . As Ar_l is of $O(1)$, V_T may be compared with Oseen's prediction. In the latter, the dimensional drag force is $6\pi\mu_2RV_T^*(1 + (3/8)Re_T)$ (Batchelor 1967), with $Re_T = \rho_2RV_T^*/\mu_2$ and $V_T^* = (\zeta_p g R)^{1/2} V_T$, which yields $V_T = (4/3)((\zeta_p - \zeta)/\zeta_p(1 + \zeta))^{1/2} Ar_l^{-1} \{-1 + (1 + Ar_l^2/3)^{1/2}\}$. As shown in figure 4(a), this prediction is in excellent agreement with the experimental and computational observations.

Figure 4(b) shows that the entrained volume of light fluid is about three times that of the sphere when the meniscus reaches its maximum depth ($z_0 \approx 2.5$). At later times, the entrained volume computed through the usual definition $\mathcal{V}_e = 2\pi \int_{z < 0} Cr dr dz$ exhibits an oscillatory behaviour, the origin of which stands in the capillary-gravity waves which develop on the interface after the meniscus has snapped. To avoid these oscillations which have nothing to do with the volume entrained by the sphere (although they are a genuine feature of the flow field), we remove the top part of the integration domain and define a modified entrained volume $\mathcal{V}_{em} = 2\pi \int_{z < -1} Cr dr dz$. Although it obviously underestimates the rise and maximum of \mathcal{V}_e for $z_0 \leq 2.5$, the evolution of \mathcal{V}_{em} agrees well with the experimental determination of \mathcal{V}_e once the meniscus has snapped, and both indicate that the sphere eventually carries a thin drop with a volume approximately $0.15\mathcal{V}$. The above agreement between the terminal velocity of the compound sphere and Oseen's prediction indicates that the drop has little net effect on the drag, which may seem surprising since its presence increases the overall buoyancy force by nearly 30 %. The reason for this lies in the large viscosity ratio ($\lambda = 18.3$): as shown by Johnson (1981), the recirculating flow within the drop, which is significant when λ is large, decreases the net drag on the compound sphere. Here it turns out that the two effects almost compensate each other.

During the stage when the sphere rises, a 'neck' forms on the meniscus (see figure 3(d,k,l), where pinch-off eventually takes place. The evolution of the neck radius, r_n , determined from experimental data, is plotted in figure 4(c) versus the

time difference $(t_p - t)/t_\gamma$, where t_p is the time at which pinch-off happens and $t_\gamma = (\rho R^3/\gamma)^{1/2}$ denotes the capillary time scale. For $(t_p - t)/t_\gamma$ of $O(1)$ or less, data are found to closely follow the power law $r_n(t) \propto (t_p - t)^{2/3}$ corresponding to the self-similar behaviour of a capillary contraction in which the fluid contained within a volume of $O(r_n^3)$ exits through a surface with an area of $O(r_n^2)$ (Marmottant & Villermaux 2004a; Eggers & Villermaux 2008).

4. The end-pinching regime

In this section, we discuss two configurations in which the sphere has enough inertia to cross the interface easily, then towing a long column of light fluid which pinches off at some point and eventually turns into a series of droplets. The regime observed in these two cases is characteristic of the evolution of the three-phase system when the viscosity ratio is in the range $0.1 \lesssim \lambda \lesssim 10$ and the relative density contrast ζ_p/ζ is significantly larger than unity.

4.1. When some more inertia makes life easier

Keeping the two fluids and the sphere size unchanged with respect to the previous subsection, we first consider the flow and interface evolution generated by the settling of a glass sphere instead of a polyacetal one (configuration 14a in PM1). Hence we still have $Bo = 1.1$, $\lambda = 18.3$ and $\zeta = 0.32$, but now $\zeta_p = 1.74$ (instead of 0.48) and $Ar = 164$ (instead of 86). As the experimental sequence in figure 5 reveals, the penetration of the sphere into the lower fluid first generates a deep, nearly cylindrical meniscus on the upper part of which a neck promptly forms (panel (c)). This meniscus still elongates, turning into a long tail which eventually pinches off at its very top under the influence of capillary effects (panel (g)), which corresponds to a ‘shallow’ pinch-off according to the terminology of Aristoff & Bush (2009). This evolution is strikingly different from the ‘rebound’ sequence observed in the previous case, underlining the influence of the sphere-to-fluid density ratio. A noticeable feature in the present experimental sequence is the non-axisymmetric geometry of the interface. This is no surprise: although the Archimedes number is fairly small in the lower fluid ($Ar_l = 9.3$), its large value in the upper fluid is well beyond the threshold $Ar_c = 55.0$ at which the path of a freely moving sphere becomes non-vertical (Fabre *et al.* 2012). Therefore the sphere does not follow a strictly vertical path before it reaches the interface and its wake is not axisymmetric, yielding a non-axisymmetric tail somewhat later. Nevertheless, the departure from axisymmetry remains moderate and the corresponding evolution is still close, at least qualitatively, to the predictions provided by axisymmetric computations, as the comparison between the two sequences in figure 5 indicates.

Here it is of interest to comment on the vorticity distribution revealed by the numerical sequence of figure 5. Examining the outer fluid along the tail, especially in snapshot (h), it is clear that the flow is almost irrotational, except in the region where vorticity generated at the sphere surface is advected upwards. In particular, vorticity remains negligibly small in that fluid along the tail, as well as below the quasi-horizontal part of the interface. This contrasts with the flow within the tail, where significant levels of vorticity are observed in snapshots (d–h). As discussed in appendix B of PM1, such a vorticity distribution results from the large viscosity contrast ($\lambda = 18.3$), which makes the flow around the tail obey virtually a shear-free condition at the interface, limiting drastically the vorticity magnitude in the outer fluid. This situation is qualitatively similar to the one observed in impact problems

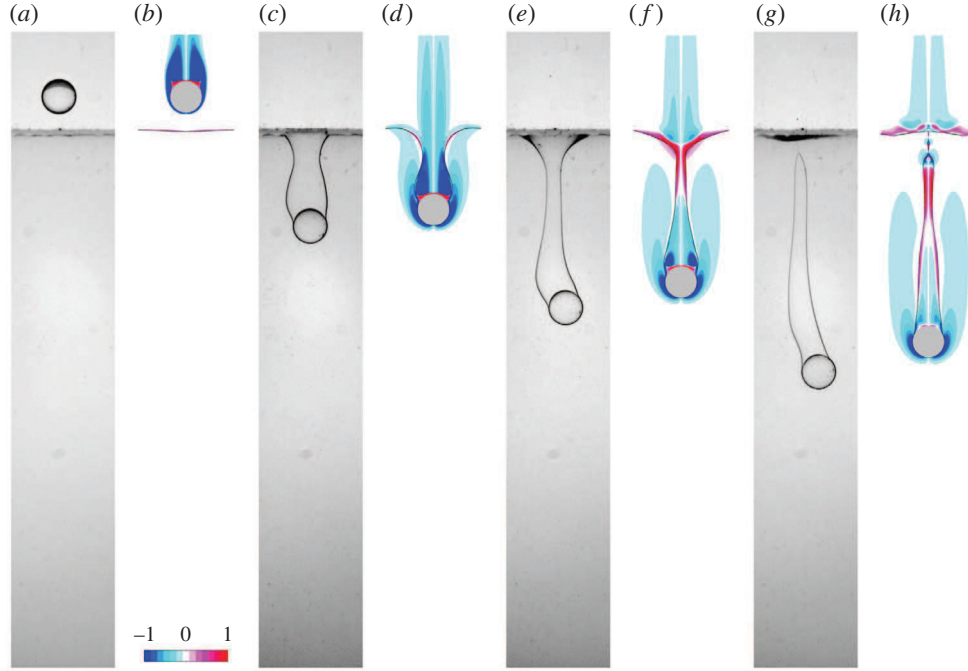


FIGURE 5. (Colour online) Passage of a 7 mm diameter glass sphere through a V5/water-glycerine interface. Experimental and computational images are taken at the same instant of time in each pair of panels; the time interval between two successive pairs is $\Delta t = 8.4$. See figure 1 for legend.

at an air–water interface, where $\lambda \approx 55$ under standard conditions. Looking at the upper fluid just above the quasi-horizontal part of the interface in snapshots (f) and (h), one notices that the negative vorticity left in the far wake of the sphere convects outwards along the interface. Simultaneously, vorticity of opposite sign is generated at the interface, around and below the expanding vortex ring. This vortex structure is reminiscent of that observed in the case of a sphere impacting a rigid wall (Thompson, Leweke & Hourigan 2007). The radial motion of the ‘old’ negative vorticity is induced by its image with respect to the wall and this radial motion in turn induces a positive shear responsible for the generation of the secondary vortex ring. The strong interaction between the two rings of opposite sign stops the outward motion a short distance from the axis. Here, the sphere is seriously slowed down as it penetrates in the lower fluid (its velocity is divided by a factor of two over a $8R$ distance) owing to the combined effect of the reduced buoyancy ($\zeta = 0.32$) and much larger viscous resistance ($\lambda = 18.3$) in the latter. Thus, although the dynamics taking place above the nearly horizontal part of the interface is less intense than if the latter were a real wall, they are similar in nature.

To save space, we do not comment in detail on the variations of the sphere velocity, entrained volume and hydrodynamic force with the vertical position, as they are qualitatively similar to those displayed in figure 9(a–c) to be discussed later. The major point is that there is no severe drop of the sphere velocity during the breakthrough, in contrast to the behaviours observed in the previous section. This is a clear indication that in the present case, capillary effects and buoyancy effects related

to entrainment of the upper fluid only play a secondary role compared to inertia. The sphere velocity reaches a maximum value $V \approx 2.15$ at $z_0 = 0$, before decreasing gently toward a terminal value $V \approx 0.8$ which is reached at $z_0 \approx 15$. This decrease results from both the large viscosity jump ($\lambda = 18.3$) and the drop of the buoyancy force experienced by the sphere once it is immersed in the lower fluid ($\zeta = 0.32$).

The late evolution of the system, after the tail separates from the flat interface, is depicted in figure 6. The initial pinch-off marks the end of the period during which the tail is stretched between the sphere and the interface. Then it behaves as a pre-elongated liquid thread embedded in a more viscous fluid, a configuration known to be prone to the development of a capillary instability (Mikami, Cox & Mason 1975). Indeed, an interfacial instability to be described below sets in and propagates downwards, generating a series of drops of decreasing size (panels (b)–(d)). Then a second pinch-off takes place just above the sphere and leaves a small drop attached to its top (in between panels (f) and (h) in the numerical sequence). This second pinch-off, which is due to buoyancy effects and corresponds to the ‘deep seal’ situation identified by Aristoff & Bush (2009), is the starting point of a second instability of the same type which propagates upwards and results in another series of drops of increasing size. Simultaneously, since buoyancy effects are significant, the daughter drops resulting from the first instability (especially the biggest ones) rise toward the flat interface. They do so with a nearly constant velocity, as may be observed by tracking the position of the biggest of them between panels (f) and (l) in the numerical sequence. They eventually coalesce with the upper fluid layer, generating a local bump on the otherwise flat interface (panel (k)). The two instability fronts get closer until the tail reduces to a string of drops, the size of which decreases with depth (panel (l) and beyond).

The situation just described is typical of the so-called ‘end-pinching’ instability of liquid threads (Stone *et al.* 1986; Stone & Leal 1989). The recession of the initial thread tip first results in a bulbous, nearly spherical end, i.e. a blob. Owing to the capillary pressure jump, the intermediate region where this blob connects to the nearly cylindrical central part of the thread corresponds to a pressure minimum, since the curvature within the thread cross-sectional plane is locally negative. If the thread viscosity is small enough compared to that of the outer fluid as it is here, this longitudinal pressure gradient drives a flow from the central cylindrical part toward this connecting region, making the pressure minimum more pronounced. This in turn forces the two radii of curvature to decrease in that region, inescapably leading to pinch-off. The process can then repeat, generating a series of daughter drops which may eventually give rise to satellite droplets (some of which are visible in the numerical sequence of figure 6) and making the cylindrical part shorten progressively. The propagation of the pinch-off process (hence of the tip position of the remaining thread) was examined from a stability viewpoint by Powers *et al.* (1998) who showed that the associated propagation speed, V_f , obeys a law of the form $V_f = k(\lambda)\gamma/\mu_2$, the pre-factor k being a slightly increasing function of λ .

Here the details of the process are somewhat more complicated than in the aforementioned studies, especially because there is a significant time lag between the two primary pinch-off events and the tail cross-section varies in a non-uniform manner from top to bottom, inducing dramatic variations in the size of the successive daughter drops generated during the process. These variations hamper a quantitative comparison of the drop size with theoretical predictions elaborated in idealized configurations. This is why we postpone it to the next subsection where the tail geometry is closer to that considered in theoretical analyses. Nevertheless, according

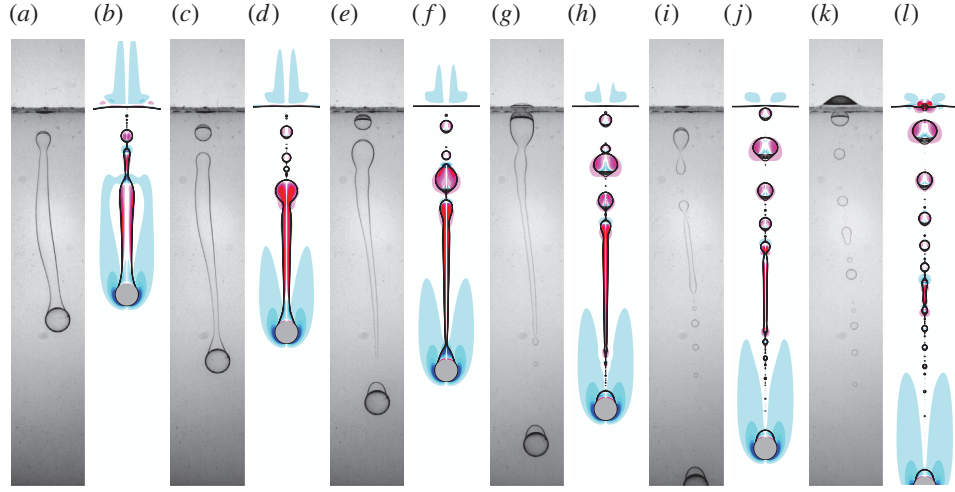


FIGURE 6. (Colour online) Late evolution of the tail in the configuration of figure 5. The time interval between two successive pairs of panels is $\Delta t = 4.15$.

to Powers *et al.* (1998), the speed at which the front of the instability propagates does not depend on the local thread radius, making a comparison of the present results with their prediction for the pre-factor k possible. From the successive positions of both the upper and lower tips of what remains from the tail (snapshots (d–h) and (h–l) respectively in figure 6), one finds $V_f \mu_2 / \gamma \approx 0.69$, which is close to the value $k(\lambda = 18.3) \approx 0.77$ determined by Powers *et al.* (1998) using boundary integral computations (see their figure 6).

4.2. An archetypal end-pinching configuration with $\lambda = O(1)$

To better explore the end-pinching regime, we now consider the situation where a 10 mm diameter Teflon sphere settles through a V50/water–glycerine set-up. The corresponding dimensionless parameters are $Bo = 1.9$, $Ar = 23.1$, $\lambda = 1.7$, $\zeta = 0.26$ and $\zeta_p = 1.25$.

The two sequences displayed in figure 7 show that the sphere penetrates into the lower fluid with only a modest velocity variation, which indicates that capillary effects play little role in the breakthrough process. A slender tail then forms and goes on connecting the sphere to the flat interface, at least up to $z_0 \approx 18$ (panels (f) and (l)). As the tail thins down, its radius is seen to exhibit a broad minimum which gets closer to the sphere (panels (d–f) and (j–l)). At the same time, the fluid contained in the upper part of the tail tends to recede toward the initial position of the interface, as the positive vorticity levels indicate (panels (j,k)). This upward motion has two important consequences. First, given the $O(1)$ viscosity ratio, a significant region of heavy fluid is entrained upwards (see the positive vorticity levels in panel (k)). This upwelling disturbs the initially flat interface, generating interfacial waves. These are clearly gravity-driven waves, as their wavelength is typically ten times the capillary length $l_c = \{\gamma / (\rho_2 - \rho_1)g\}^{1/2}$. Second, owing to the negative (i.e. downward) pressure gradient this flow induces along the tail, the mean curvature at the top has to decrease to satisfy the normal stress balance. As explained in the previous subsection, this yields the formation of a neck at the junction between the tail and the (almost)

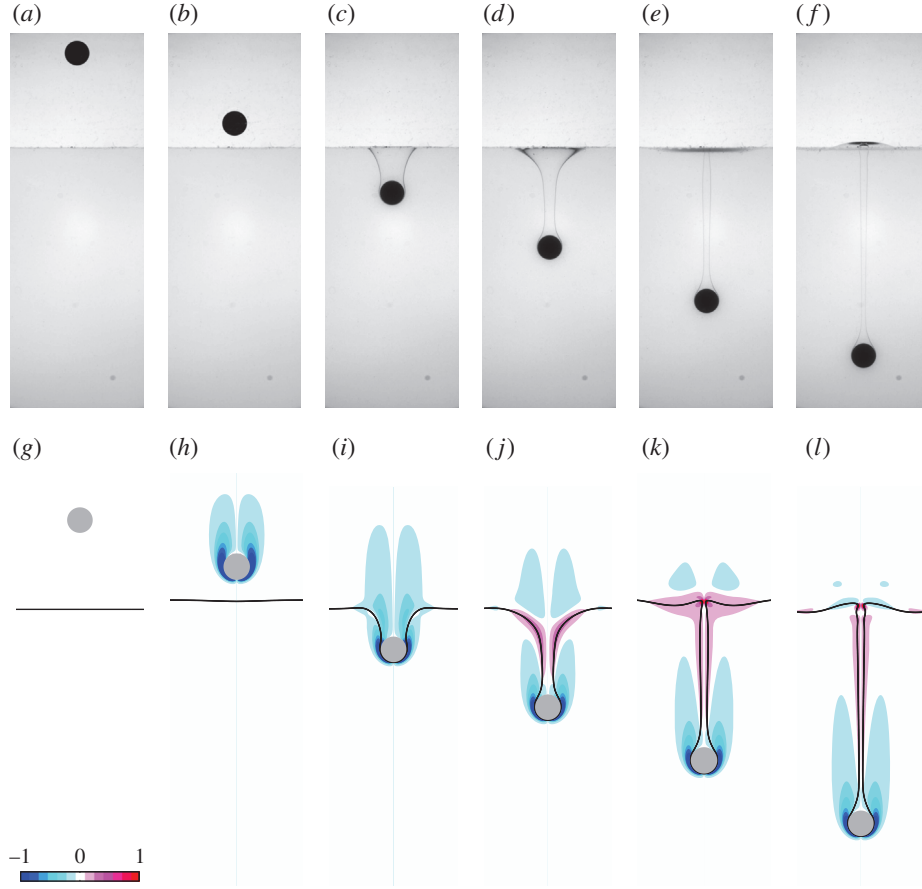


FIGURE 7. (Colour online) Passage of a 10 mm diameter Teflon sphere through a V50/water-glycerine interface. Experimental (*a–f*) and numerical (*g–l*) sequences; the time interval between two successive frames in each sequence is $\Delta t = 5.0$. See figure 1 for legend.

horizontal interface (panels (*e,f*) and (*k,l*)). Considering the situation in the last stage of figure 7, one could guess that pinch-off is going to take place at this neck. This is actually not the case, as the computational sequence displayed in figure 8 reveals. This sequence enlightens the strong coupling existing between the evolution of the neck radius and that of the vertical displacement of the wavy part of the interface: as panels (*a–c*) (respectively (*d–f*)) show, the latter experiences an upward (respectively downward) motion throughout the stage during which the neck shrinks (respectively re-opens). This one-to-one coupling may be readily understood by noting that the time rate-of-change of the interfacial energy is $(d/dt) \int_{S_I} \gamma dS = \gamma \int_{S_I} (\nabla \cdot \mathbf{n})(\mathbf{u} \cdot \mathbf{n}) dS$, while that of the potential energy is $-(1/2)(\rho_2 - \rho_1)g(d/dt) \int_{S_I} z^2 (\mathbf{n} \cdot \mathbf{e}_z) dS$, where S_I denotes the surface separating the two fluids and \mathbf{n} is directed towards the interior of the lower fluid. Hence, neglecting dissipative effects and variations of the kinetic energy over the whole fluid volume, when the neck narrows ($\mathbf{u} \cdot \mathbf{n} < 0$), the interfacial energy decreases (since the mean curvature $\nabla \cdot \mathbf{n}$ keeps a positive sign), and this decrease is essentially balanced by the upward displacement of the nearly horizontal

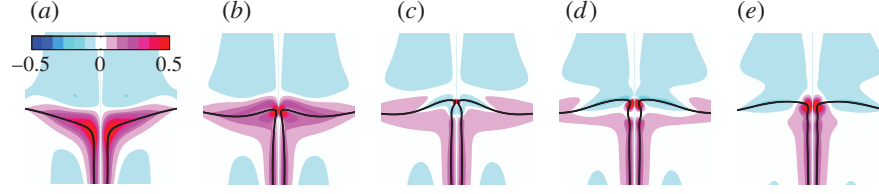


FIGURE 8. (Colour online) Zoom of a computational sequence showing the re-opening of the neck at the top of the tail; the time interval between two successive panels is $\Delta t = 2.5$.

part of the interface (on which the vertical component $\mathbf{n} \cdot \mathbf{e}_z$ of the normal is negative). However, the upward flow rate through the neck decreases as the neck radius goes to zero, which at some point stops the ‘feeding’ of the light fluid layer by the tail. The restoring effect of the density difference $\rho_2 - \rho_1$ then drives a downward motion of the near-axis region of the wavy interface (figure 8c–e), thus lowering the potential energy and allowing the interfacial energy to increase through a re-opening of the neck ($\mathbf{u} \cdot \mathbf{n} > 0$). This is how the tail escapes from pinching thanks to the restoring effect of the buoyancy force. This escape process is totally different from that identified by Hoepffner & Paré (2013) in the case of an isolated receding liquid thread, where the key mechanism is the detachment of a vortex ring from the neck, which propagates toward the tip (i.e. through the blob) and creates a pressure loss therein.

The variations of V , \mathcal{V}_e and F throughout the range of vertical positions of the sphere considered up to now are plotted in figure 9. Owing to the limited height of the tank, the sphere does not reach its terminal velocity before touching the interface, which is why V and F go on increasing until it reaches the position $z_0 \approx -1$ (using an empirical drag law, the terminal velocity in an unbounded fluid may be approximately estimated to 1.42). The mild decrease of V in the range $-1 \leq z_0 \leq 8$ is mostly due to the fluid density contrast and, to a lesser extent, to the slightly larger viscosity of the lower fluid. Indeed, balancing the drag force with the net weight of the sphere and assuming the drag coefficient to be the same in both fluids, the ratio of the terminal velocities in the lower and upper fluids would be $((\zeta_p - \zeta)/\zeta_p(1 + \zeta))^{1/2} \approx 0.79$, whereas if the sphere were settling in the Stokes regime, this ratio would be $(\zeta_p - \zeta)/\lambda\zeta_p \approx 0.58$. According to figure 9(a), the ratio $V(z_0 = 20)/V(z_0 \approx 0) \approx 0.73$ lies in between these two estimates, which supports the above view. Perhaps the most interesting feature in that figure is the minimum of V which may be observed at $z_0 \approx 8$, corresponding to the situation of figure 7(d,j). Estimates of the static forces discussed in §4 of PM1 indicate that at this position (where the cap angle is approximately $2\pi/3$), the tail-induced buoyancy force is approximately 4.2 times larger than the buoyancy force acting on the sphere itself, whereas the capillary force plays virtually no role. Hence the observed minimum is a direct consequence of the maximum reached by the volume of the tail at this position. This prediction is confirmed in figure 9(b) where it is seen that the entrained volume $\mathcal{V}_e - 1$ goes through a maximum value about 6.0 at $z_0 \approx 8$. As already observed in figure 4(b), the computational prediction greatly overestimates the tail volume at larger depths, as it becomes dominated by the contribution of the interfacial wave system which develops when $z_0 \geq 11$. Figure 9(c) shows that the force acting on the sphere experiences a significant bump when $-1 \leq z_0 \leq 8$. A crude reasoning considering that, when the sphere crosses the position $z_0 = 0$, half of it is immersed in each fluid and there is no meniscus (i.e. $\psi = \pi/2$), indicates that the corresponding

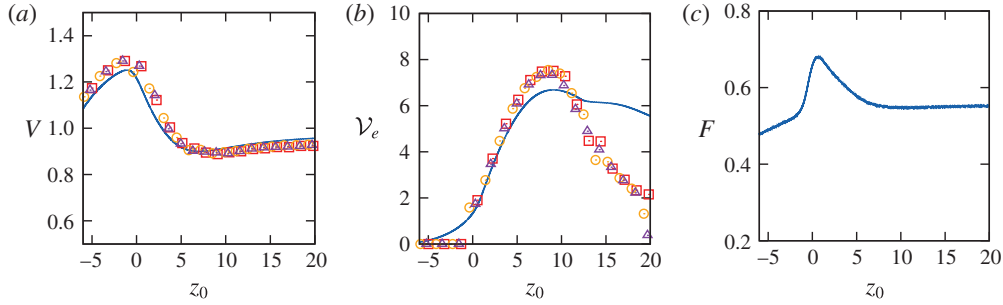


FIGURE 9. (Colour online) Evolution of three characteristics of the configuration considered in figure 7: (a) settling velocity $V(z_0)$; (b) displaced volume $\mathcal{V}_e(z_0)$; (c) effective drag force $F(z_0)$. For legend, see figure 4.

contribution of the capillary force should be approximately 0.09, while that of the extra buoyancy force due to the fluid density contrast should be approximately 0.06. These estimates predict an increase of the total force about 0.15 at $z_0 = 0$, in good agreement with the computational result.

Figure 10 shows how the tail evolves after its very top escaped from pinching. Whilst the sphere goes on settling, the lower part of the tail becomes very thin and pinch-off eventually takes place near the top of the sphere, which is then released in the lower fluid with an attached drop about one-third its own volume. An end-pinching sequence starts and propagates upward, generating larger drops as the front rises, owing to the increasing tail radius (panels *b,d*). In panel (*d*), satellite droplets are seen to form in between the daughter drops. Moreover, capillary waves associated with the Rayleigh–Plateau instability propagate ahead of the front. Throughout this stage, the upper half of the tail still recedes toward the horizontal part of the interface and a new neck starts to form at its very top (panels *a,b*). However the tail is now much thinner than it was in figure 7(*j–l*). Consequently the upward flow rate is much smaller and barely disturbs the horizontal interface. This is why the previously described restoring buoyancy mechanism is no longer able to stop the shrinking of the neck and a new pinch-off takes place at the top of the tail just after panels (*c,d*). A second end-pinching front then propagates downward. Thus the remaining slender ligament still present in panels (*e,f*) quickly breaks almost symmetrically from both extremities (panels *g,h*), generating a new series of daughter drops and satellites.

The formation of satellite droplets is known to occur in between daughter drops, either due to the classical capillary wave instability mechanism or, as is the case here, to the end-pinching process which takes place along the cylindrical ligament left after a daughter drop has formed at each of its extremities. It has been shown to be a self-repeating process in which the larger λ the larger the number of successive generations of satellites (Tjahjadi, Stone & Ottino 1992). Unfortunately, neither the resolution of the camera nor that of the computational grid allows us to draw firm conclusions on this dependence from figures 6 and 10. It is much easier to compare the characteristic size of the observed daughter drops with theoretical predictions provided by linear stability theory. In the situation of interest here, namely a nearly cylindrical viscous thread surrounded by another viscous fluid at rest, the relevant theory was established in the Stokes flow limit by Tomotika (1935). Provided the density contrast between the two fluids is small and the viscosity ratio is of $O(1)$, his

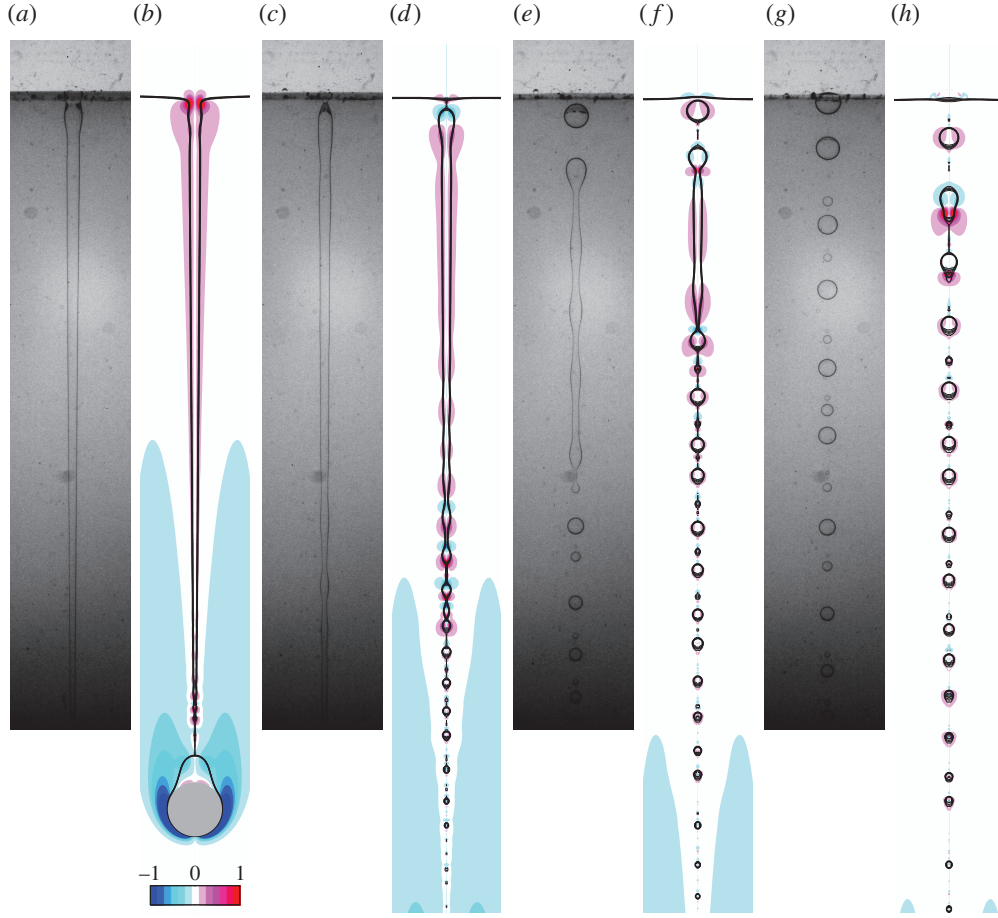


FIGURE 10. (Colour online) Late evolution of the tail in the configuration of figure 7. The time step between two successive panels is $\Delta t = 7.4$.

results indicate that the wavelength of the most amplified eigenmode, Λ , normalized by the thread radius, R_t , depends only on λ . Specifically, for $\lambda = 1.7$, his theory predicts $\Lambda/R_t \approx 10.65$. Assuming that the growth of this mode eventually leads to the breakup of Λ -long cylindrical pieces, each of which turns into a spherical drop, the radius R_d of these drops is expected to be $R_d = ((3/4)\Lambda R_t^2)^{1/3}$, so that $R_d/R_t \approx 2.0$ for $\lambda = 1.7$. Here the tail is not cylindrical but has a slowly varying cross-section. Hence, in the present context, the above prediction must be considered as local, assuming that R_d and R_t vary slowly with the position along the tail. Considering the tail geometry just prior to the initial pinch-off in figure 10(a,b), figure 11 shows how the size of the drops identified in the experimental and computational sequences compare with Tomotika's prediction. The lower group of data must be excluded from that comparison because it corresponds to satellite droplets, the formation of which is driven by nonlinear processes (Tjahjadi *et al.* 1992). The rest of the data display good agreement with the linear prediction, although the computational series exhibits a somewhat smaller slope, presumably because of marginally sufficient resolution. Interestingly, the inviscid linear theory (Rayleigh 1878) predicting $\Lambda/R_t \approx 9.02$, i.e.

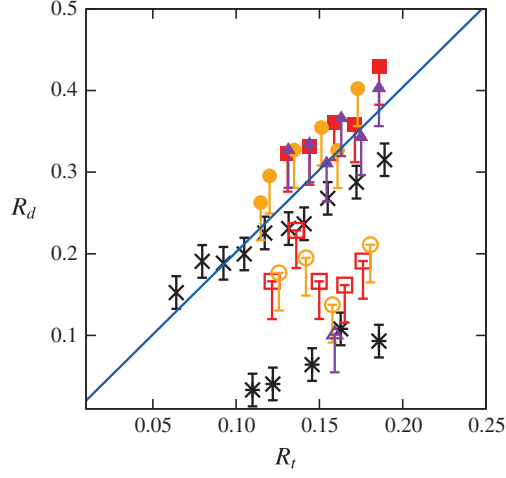


FIGURE 11. (Colour online) Variation of the drop radius versus the local tail radius (both normalized by R). Solid line: theoretical prediction (Tomotika 1935); \times , $*$: numerical results for the primary and satellite drops, respectively, the error bars correspond to ± 1 grid cell; close (respectively open) symbols: experimental results for the primary (respectively satellite) drops, the error bars correspond to ± 3 pixels.

$R_d/R_t \approx 1.89$, it is observed that the stabilizing effect of viscosity increases the drop size by only 6% in the present case.

5. Sinking in a low-viscosity fluid

In this section we consider two situations belonging to figure 5(b) of PM1 in which inertia effects are fairly modest in the upper fluid but become large in the lower one, owing to the huge viscosity contrast of the V500/water pair of fluids. Hence the tail develops within a nearly inviscid fluid. A noticeable feature in these configurations is that the sphere goes on settling vertically during the whole observation period, although the Archimedes number Ar_l characterizing its motion within the lower fluid is well beyond the path instability threshold known for a homogenous fluid ($Ar_c = 55.0$). As already explained in 3.3 of PM1, the reason for this is that the relevant ratio between inertia and viscous effects to assess the stability of the sphere path and wake is the one involving the viscosity within the tail. Even though the terminal velocity of the sphere in the lower fluid, say V_{l2} , may be up to four times that in the upper fluid as we shall see, this increase is not large enough for the Reynolds number $\rho_1 V_{l2} R / \mu_1$ to reach the threshold corresponding to path instability, thus keeping the straight vertical path stable. Hence the only instabilities to be expected in the regimes examined below are those which may develop at the interface between the two fluids.

5.1. An archetypal retraction process with $Ar_l = O(10^3)$

We start by examining the settling of a 10 mm diameter Teflon sphere. This situation, close to that corresponding to configuration 23b in figure 5(b) of PM1, is characterized by dimensionless parameters $Ar = 2.3$, $Bo = 0.24$, $\lambda = 1.9 \times 10^{-3}$, $\zeta = 0.03$ and $\zeta_p = 1.23$, hence $Ar_l \approx 1.19 \times 10^3$.

Although the Bond number is small, figure 12(b,h) indicates that the interface starts to deform well before the sphere reaches it. This is no surprise: given the modest

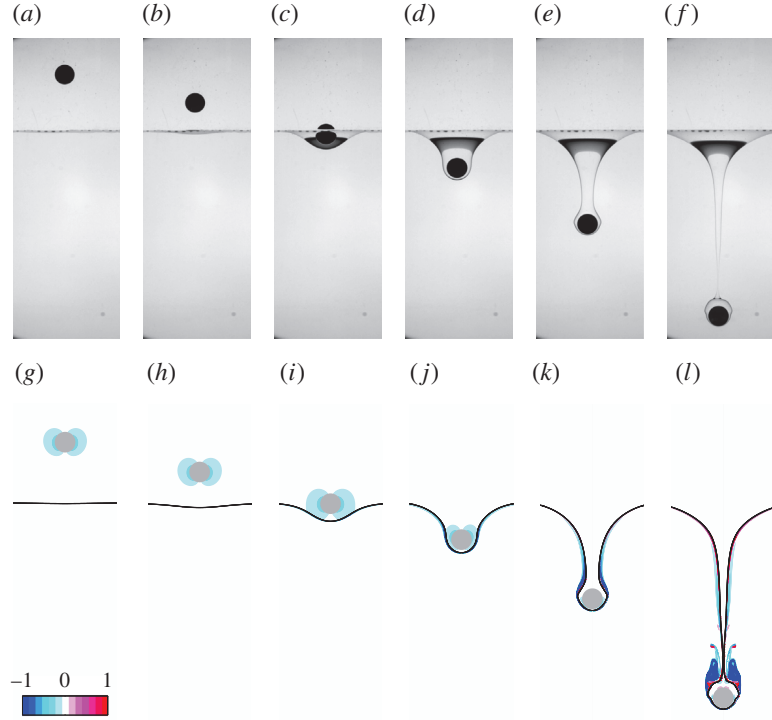


FIGURE 12. (Colour online) Settling of a 10 mm diameter Teflon sphere through the V500/water pair of fluids. Experimental (*a–f*) and numerical (*g–l*) sequences; the time interval between two successive panels in each sequence is $\Delta t = 4.5$. See figure 1 for legend.

value of Ar , the spatial structure of the flow disturbance in the upper fluid is close to that corresponding to the Stokes limit, as confirmed by the approximate fore–aft symmetry of the vorticity field in figure 12(*g,h*). Hence the leading contribution to the velocity disturbance decays as the inverse of the distance to the sphere position (Lee, Chadwick & Leal 1979), making it able to bend the interface significantly as soon as $|z_0| \lesssim 5$. The Bond number being small, surface tension effects tend to maintain the deformed part of the interface broad in order to limit the increase of the interfacial energy. This contrasts with figure 7 where the Bond number is an order of magnitude larger, then allowing the development of a much more localized deflected region. The entrained column lengthens gradually and thins above the sphere. Pinch-off eventually takes place when $z_0 \approx 20$, leaving the top part of the sphere covered with a thick spherical cap droplet, the front part being still encapsulated in a thin film (figure 12*f,l*). As may be seen in snapshots (*i–k*), the large viscosity contrast forces the velocity profile within any cross-section of the tail to become nearly flat, reducing gradually the magnitude of the vorticity around the sphere. In snapshot (*k*), the diameter of the column is still of the same order as that of the sphere, and vorticity is essentially concentrated within a thin shear layer surrounding the bottom part of the tail. It reaches its maximum just above the sphere, since the straining of the column makes the velocity of the entrained fluid maximum there. Things become different when pinch-off is about to occur (snapshot *l*). At that stage, the compound body made of

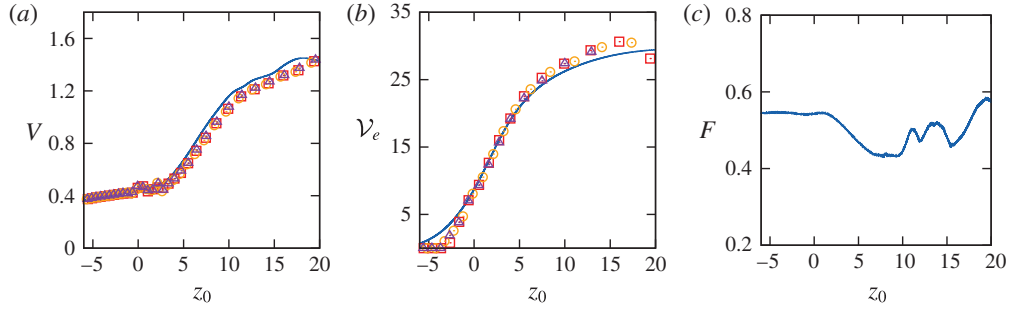


FIGURE 13. (Colour online) Evolution of three characteristics of the configuration considered in figure 12: (a) settling velocity $V(z_0)$; (b) displaced volume $\mathcal{V}_e(z_0)$; (c) effective drag force $F(z_0)$. For legend, see figure 4.

the sphere and the drop that encapsulates it falls within the lower, low-viscosity fluid, maintaining a connection with the rest of the column only through a very thin thread. Therefore the wake which develops past the sphere is essentially similar to that past a freely translating nearly spheroidal bluff body. The corresponding Reynolds number is approximately 2.6×10^3 , which of course promptly results in the development of a large separated wake.

Figure 13(a) shows that the sphere velocity remains almost unaltered by interfacial effects up to $z_0 \approx 3$. Beyond that point, the sphere experiences a strong acceleration, tripling approximately its velocity between $z_0 = 3$ and $z_0 = 11$. Then, the settling velocity increases more slowly, reaching its terminal value shortly after pinch-off occurs at the bottom of the tail. The ratio of the terminal velocity in the lower fluid to that in the upper one is about 3.2, close to the approximate prediction 3.4 provided by (A3) of PM1. As shown by figure 13(b), fluid entrainment below the initial level of the interface starts significantly before the sphere has reached the corresponding position, owing to the low-Reynolds-number behaviour already pointed out. Then the entrained volume goes on increasing regularly and reaches a maximum value approximately 30 times the sphere volume. This maximum takes place before pinch-off occurs, which is not unlikely since the upper part of the column has already started to recede at that time. The force experienced by the sphere (figure 13c) is seen to decrease sharply in the range $2 \leq z_0 \leq 7$, owing to the small friction exerted by the low-viscosity outer fluid on the very viscous tail. This results in an increase of the sphere velocity, hence of the aforementioned friction, so that the force stops decreasing after some time and exhibits a ‘plateau’ in the range $7 \leq z_0 \leq 10$. The development of the sphere wake for $z_0 > 10$ (i.e. in between panels (k) and (l) of figure 12) increases the energy dissipation in the outer fluid near the top of the sphere, which, on average, yields an increase of the force until it recovers a level close to its initial value. Nevertheless, oscillations due to transient effects affecting the wake, especially the release of vortex rings and the retraction of the bottom part of the column (see figure 14 below), are seen to take place during that stage.

Pinch-off takes place close to the sphere when $z_0 \approx 22$. As may be discerned in figure 14(a), just before it occurs, the bottom part of the very thin thread that still connects the column to the drop covering the sphere is no longer axisymmetric and exhibits some bending. Although this asymmetry is reminiscent of the coiling of viscous filaments (Ribe, Habibi & Bonn 2012), we believe that it is a manifestation of the three-dimensional effects which develop in the sphere wake, owing to the

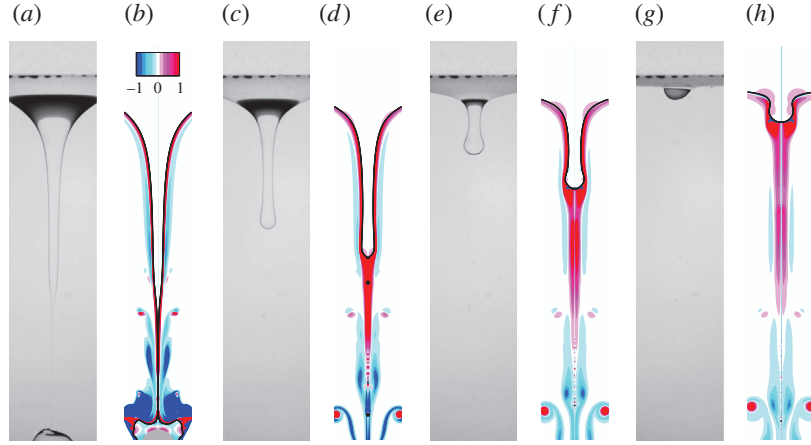


FIGURE 14. (Colour online) Near- and post-pinch-off evolution of the tail; $\Delta t = 6.0$.

current large Reynolds number. After pinch-off happens the initially conical thread starts to recede and capillary effects quickly turn its tip into a blob (figure 14*c,d*). The now nearly cylindrical thread thickens and continues to recede (figure 14*e–h*) until it eventually disappears, leaving the two fluids separated by a flat interface. In contrast to the situations examined in the previous section, no end-pinching instability happens during this recession. This is in line with previous findings which showed that, in cases where $\lambda \ll 1$, the formation of a neck in the tip region is slowed down by the inner resistance of the thread, making the blob capable of receding fast enough to prevent the thread from breaking (Stone *et al.* 1986; Stone & Leal 1989).

The velocity V_B at which the tip recedes, still normalized by $(\zeta_p g R)^{1/2}$, is plotted as a function of its position in figure 15. After an initial deceleration (when $z_0 \gtrsim 9$), experimental and numerical data exhibit a clear ‘plateau’ with $V_B \approx 0.75$ in the range $4 \lesssim z_0 \lesssim 9$. In the late stage ($z_0 \lesssim 4$), the residual column thickens rapidly as it shortens, making the retraction velocity decrease sharply over time. The intermediate plateau is reminiscent of the Taylor–Culick inviscid prediction (Taylor 1959; Culick 1960), according to which the capillary-driven retraction velocity of a planar sheet having a uniform thickness \mathcal{R} is $V_{TC} = (2\gamma/(\rho_1 \mathcal{R}))^{1/2}$. Later, this analysis was extended to cylindrical threads by Keller (1983) who concluded that the same result still applies, \mathcal{R} then being the thread radius. However, it was recently pointed out (Hoepffner & Paré 2013) that the correct velocity in that case is actually $V_{TC} = (\gamma/(\rho_1 \mathcal{R}))^{1/2}$. This prediction is confirmed in appendix C using a more general argument based on an exact momentum balance over the entire column, similar to that employed by Savva & Bush (2009) for a planar sheet. In particular, the above result is shown to hold in the presence of viscous effects, provided several conditions are satisfied. The corresponding prediction is plotted in figure 15 and is seen to underestimate the actual velocity during the plateau by more than 40%. The analysis developed in appendix C reveals that buoyancy effects due to the density difference between the two fluids are responsible for this disagreement, their magnitude being similar to that of capillary effects. An extended version of the Taylor–Culick prediction including both effects is derived in (C 10). At short time, the modified retraction velocity is shown to be $V_{TCg} = (\zeta g \mathcal{L}_0 + \gamma/(\rho_1 \mathcal{R}))^{1/2}$, \mathcal{L}_0 denoting the initial length of the column. Hence the two effects cooperate in a simple manner to strengthen the retraction process, and

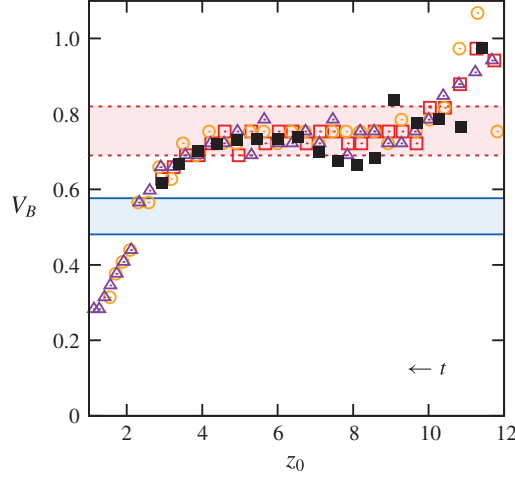


FIGURE 15. (Colour online) Evolution of the normalized retraction velocity V_B of the tip of the tail as a function of its position. Dotted squares, triangles and circles refer to three different sets of experimental data, while closed squares refer to computational results. Lower horizontal band: original Taylor–Culick prediction with an average thread radius \mathcal{R}_m ranging from $0.4R$ (bottom line) to $0.3R$ (top line); upper band: prediction including buoyancy effects, with the same two extreme values of \mathcal{R}_m and an initial length of the column ranging from $\mathcal{L}_0 = 10R$ (bottom line) to $\mathcal{L}_0 = 15R$ (top line); see appendix C for the determination of \mathcal{R}_m and \mathcal{L}_0 .

the longer the column the larger the buoyancy contribution. As figure 15 reveals, this prediction is in excellent agreement with observations. Keeping in mind that $\zeta = 0.03$ in the present case, the 40 %–50 % difference between V_{TC} and V_{TCg} emphasizes the prominent role played by buoyancy effects, even with modest density contrasts, in the retraction dynamics.

5.2. Increasing Ar_l again

In this last case, we keep the same fluids arrangement as in the previous subsection but consider a bigger ($R = 7$ mm) and heavier (steel) sphere, which yields Bond and Archimedes numbers two and four times larger, respectively; this is the most inertial situation displayed in figure 5(b) of PM1 (configuration 27b). The corresponding dimensionless parameters are now $Bo = 0.46$, $Ar = 9.2$, $\lambda = 1.9 \times 10^{-3}$, $\zeta = 0.03$ and $\zeta_p = 7.15$, so that $Ar_l \approx 4.8 \times 10^3$.

In the early stages, the dynamics of the flow is very similar to that observed in the previous case. Note however that the film ahead of the sphere is drained significantly faster (compare panels (c) and (h) in figure 16 with panels (d) and (j) in figure 12). This is a direct consequence of the larger sphere inertia which yields a larger velocity at the interface of the two fluids, making the drainage easier (the thickness of the film at a given time is expected to vary as $\zeta_p^{-1/2}$ when $\zeta \approx 0$ (Hartland 1968, 1969)). The most spectacular novelty compared to the previous case occurs somewhat later, when disturbances are seen to propagate upward along the interface at the back of the sphere, generating a series of thin axisymmetric corollas or ‘inverted skirts’ around the core of the column while the latter remains attached to the sphere (panels (d,e) and (i,j)). Similar observations in the same pair of fluids were reported with

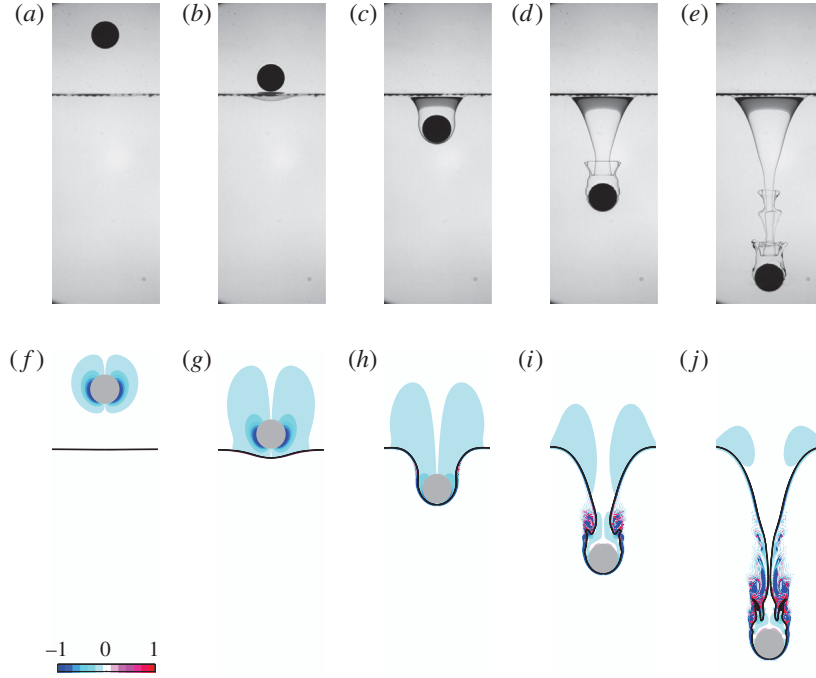


FIGURE 16. (Colour online) Settling of a 14 mm diameter steel sphere through the V500/water pair of fluids. Experimental (a–e) and numerical (f–j) sequences; the time interval between two successive panels in each sequence is $\Delta t = 4.5$. See figure 1 for legend.

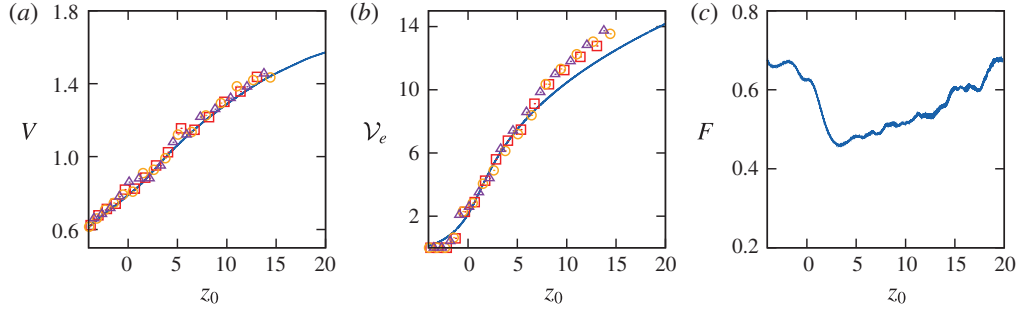


FIGURE 17. (Colour online) Evolution of three characteristics of the configuration considered in figure 16: (a) settling velocity $V(z_0)$; (b) displaced volume $V_e(z_0)$; (c) effective drag force $F(z_0)$. For legend, see figure 4.

large ceramic spheres by Kemiha (2006) (see Dietrich, Poncin & Li 2011). The vorticity distribution around these corollas (panels (i,j)) reveals an alternation of strong positive and negative values, which is indicative of an intense generation of small-scale vortices. Visually, the phenomenon is reminiscent of the early stages of the disintegration of a cylindrical liquid jet peeled off by a fast coaxial gas stream (Marmottant & Villermaux 2004b). We shall see later up to which point the analogy holds.

Figure 17(a) shows that, owing to its large inertia, the sphere accelerates throughout the whole range of positions corresponding to the viewing window (due to the limited height of the device, its velocity is only approximately 75 % of the terminal value when $z_0 = 0$). The settling velocity experiences a mild regular increase and displays no signature of an additional resistance when the sphere crosses the initial position of the interface, nor of a sudden increase below it, in contrast to the behaviour observed in figure 13(a). This is an indication that, throughout the sphere descent, inertia effects are large enough for the drag force to depend only weakly on the fluid viscosity. The displaced volume (figure 17b) obeys a similar evolution. It is noticeable that its ‘final’ value at $z_0 = 20$ is about half that found in figure 13(b). Again this is an effect of the larger sphere inertia which, for a given z_0 , reduces fluid entrainment, yielding a somewhat thinner column, especially in the top region which contributes most to \mathcal{V}_e (compare for instance figures 16(c) and 16(d) with figures 12(d) and 12(e), respectively). The small divergence between the experimental and numerical determinations of \mathcal{V}_e observed for $z_0 \gtrsim 7$ arises because the entire volume of fluid enclosed within the corollas artificially contributes to the entrained volume in the former, the weak optical contrast between the two fluids preventing the image processing software from discriminating them properly in that region. The mechanisms governing the evolution of the effective drag force displayed in figure 17(c) are essentially similar to those discussed in the previous subsection but two noticeable differences have to be mentioned. First, the nearly six times larger solid-to-fluid density contrast yields an approximately four times larger maximum sphere acceleration, $(d|V|/dt)_{\max} \approx 0.5g$ for $z_0 \approx 3$, which results in a larger drop of the force. Second, the wake develops more rapidly (see figure 16i) which corresponds to $z_0 \approx 7$, making F again increase as soon as $z_0 \gtrsim 4$, without any significant intermediate plateau.

Figure 18 displays a sequence revealing the various stages of the formation of corollas in the bottom part of the tail (the whole sequence takes place in between panels (c) and (e) of figure 16). At the very beginning, bumps are seen to form at the interface along the rear half of the sphere, quickly yielding a highly visible ring-like protrusion at its back. The top part of this protrusion then starts to hollow out and stretch in the vertical direction, giving rise to a well-defined corolla. During that time, new bumps form at the interface along the sphere, even on its front part, exhibiting crenel-like shapes with sharp angles. Once a bump has reached the top of the sphere and has transformed into a protrusion, a new corolla starts to form. Hence, after some time, the central column is surrounded by an annular region of heavy fluid which itself is surrounded by a series of thin corollas, the lowest corolla and the tail remaining connected just at the back of the sphere.

Several generic instability mechanisms may be suspected to drive the generation of this remarkable tail geometry. They may in principle be discriminated by comparing their growth rates at the most amplified wavenumber, i.e. the one corresponding to the separation distance between two successive bumps during the early stage of the instability (approximately in the second panel of figure 18). Such a comparison is attempted in appendix D. The Rayleigh–Taylor mechanism is easily ruled out because the observed wavenumber is found to lie far beyond the capillary cutoff, owing to the large capillary length. Although the strongly non-parallel geometry of the flow past the sphere may partly hamper application of classical theoretical predictions, a simple three-layer inviscid model with a piecewise linear velocity profile is then developed to examine the relevance of the Kelvin–Helmholtz mechanism. Crucial in this model is the thickness of the boundary layer in the outer fluid, which we evaluate as a function

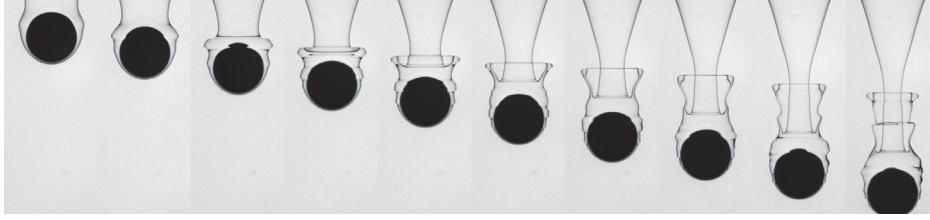


FIGURE 18. Sequence showing the development of the corollas at the back of the sphere. The time step between two successive images is $\Delta t = 0.6$. Note that, although each image corresponds to a side view, the corollas are thin enough for light to cross them and reveal their inner contour, together with the shape of the central column.

of the vertical position of the sphere by analogy with the growth of the viscous layer in Stokes' first problem. Incorporating capillary effects into the dispersion relation, we find that the most amplified wavenumber predicted by this model closely matches visual observations. In the situation considered in § 5.1, a precursor bulge is also clearly visible on the interface near the sphere equator (panels (e,k) in figure 12) but no instability develops subsequently. In that case, the same model predicts that capillary effects are strong enough to damp the initial disturbance. These predictions give strong support to the scenario based on the Kelvin–Helmholtz mechanism. In appendix D we also examine the possibility of a viscous instability due to the large viscosity difference between the two fluids. It turns out that no theoretical result is currently available to predict the behaviour of this type of instability in the present configuration, owing to the broad range of characteristic length scales induced by the huge viscosity contrast. Nevertheless, results of two numerical investigations of the linear instability problem (Boeck & Zaleski 2005; Otto, Rossi & Boeck 2013), where the behaviour of inviscid and viscous modes was compared for various fluid density contrasts, indicate that the inviscid mode dominates when $\lambda \ll 1$ and $\zeta \rightarrow 0$, which corresponds to the present conditions. Hence all arguments concur to conclude that the mechanism that initiates the observed corollas is a Kelvin–Helmholtz instability.

We note that there is now a general consensus that this instability is also at the root of the primary stage of the disintegration of a liquid jet by a fast gas stream, although the role of viscous effects is still in debate (Otto *et al.* 2013; Matas 2015). Nevertheless, a crucial difference occurs during the next stage. In the latter case, interfacial protrusions are accelerated in the streamwise direction by the high gas velocity, resulting in a Rayleigh–Taylor instability which has been identified as responsible for the formation of longitudinal ligaments (Marmottant & Villermaux 2004b; Eggers & Villermaux 2008). Here, as already discussed in § 6 of PM1, the capillary length is large, making the Rayleigh–Taylor mechanism unable to amplify azimuthal disturbances within the tail. Wake instability being the only significant source left for axial symmetry breaking, corollas preserve their axisymmetry even during the late stages of their evolution, as seen in figure 16(e), until the first three-dimensional structures resulting from this instability occur in the near wake.

6. Summary and concluding remarks

We used a combination of experiments and computations to explore the axisymmetric dynamics that takes place under certain conditions when a rigid sphere settles through a two-layer system made up of two superimposed immiscible Newtonian fluids. We

considered a wide range of conditions, from slow breakthrough situations controlled by film drainage and meniscus instability, to inertia-dominated configurations where remarkable skirt-like structures develop at the surface of the column pulled by the sphere.

We started with two configurations in which the interface represents a real barrier to the sphere settling, owing to the dominant influence of capillary and buoyancy effects. In § 3.1, the sphere descent in the upper fluid was governed by viscous effects. The sphere was virtually stopped at the interface for a long time, during which the film around it was drained in a quasi-static manner; after the meniscus snapped, the sphere was finally released in the lower fluid with a small drop attached to its top, the presence of which significantly increases the overall buoyancy force. In the second case (§ 3.2), the sphere reached the interface with a significant kinetic energy and was followed by a well-developed wake. Then, although a static approach suggests that it should remain trapped at the interface, it was found to eventually cross it after a complex process including a transient ‘levitation’ stage during which it rose toward the interface. We showed that this intriguing behaviour is due to the collapse of the wake, the sphere being severely decelerated at the interface, owing to the significant density contrast between the two fluids and large viscosity of the lower fluid.

In all other situations considered here, the sphere-to-fluid density contrast was sufficient for the sphere to cross the interface without being appreciably slowed down by capillary effects. Under such conditions, the breakthrough is always achieved through a ‘tailing’ configuration. The maximum of the tail volume is dramatically influenced by the density contrast and viscosity ratio. When the two fluid densities are close and/or the viscosity of the lower fluid is small, the entrained volume may be very large (up to thirty times the sphere volume) because fluid elements located below the interface displace and deform easily, allowing the top part of the tail to adopt a flared conical shape which provides a large contribution to the entrained volume. Conversely, only relatively thin cylindrical columns can develop when the density contrast is significant and/or the viscosity of the lower fluid is large, yielding much smaller entrained volumes (only up to 6–7 times the sphere volume in the situations examined here). This geometrical difference also influences the position of the primary pinch-off, as already discussed in PM1: the tail breaks close to the sphere (deep seal) when the top region of the column is conical, and generally at its very top when it is nearly cylindrical (shallow seal). For moderate sphere-to-fluid density ratios, the switch between these two locations takes place when the two fluids have comparable viscosities. In that case, a subtle competition between antagonistic mechanisms may take place, as seen in § 4.2 where the neck that forms at the top of the tail eventually re-opens thanks to energy transfer from interfacial waves present on the nearly flat part of the interface.

Once the tail has pinched off at one of its extremities, it behaves as a pre-elongated axisymmetric liquid thread relaxing under the combined effect of capillary, viscous and buoyancy forces. When the viscosity of the outer fluid is larger than or of the same order as that of the inner one (§ 4), the tail experiences an end-pinching instability. Actually, since its two extremities do not pinch off simultaneously, two successive end-pinching sequences propagate in opposite directions, resulting in the formation of a series of daughter drops, with satellite droplets in between two successive drops. When the longitudinal variation of the tail radius is moderate, the size of the daughter drops compares well with the predictions of the classical Rayleigh–Tomotika linear theory (§ 4.2).

When the outer fluid is much less viscous than the inner one, the tail recedes as a whole and no noticeable neck forms in the tip region. After a deceleration stage, the

velocity at which this tip recedes exhibits a clear ‘plateau’ reminiscent of the inviscid Taylor–Culick regime (§ 5.1). However, this velocity was found to significantly exceed the classical prediction. Using overall mass and momentum balances (appendix C), we showed that capillary and buoyancy effects combine in an additive manner to increase the tip velocity, and the larger the initial length of the column the stronger the buoyancy contribution.

Still in the case where the tail is much more viscous than the outer fluid, but only for large enough sphere inertias, thin axisymmetric corollas or ‘inverted skirts’ grow behind the sphere and propagate upwards well before the tail breaks. As the regime map in § 3.3 of PM1 made clear, this peculiar interfacial structure represents the last axisymmetric step before three-dimensional fragmentation occurs. We showed that shear instability is the most likely mechanism to explain the generation of these corollas and explored this possibility by considering an inviscid model in which uniform flows within the tail and in the outer fluid are separated by a thin boundary layer surrounding the interface (appendix D). In the configuration examined in § 5.1, no corollas take place and the model correctly predicts that all disturbances are damped by capillary effects. Conversely, in the case where corollas are observed (§ 5.2), the model predicts a positive maximum growth rate and a corresponding wavelength which agrees well with observations. These results strongly support the view that the fragmentation process is initiated by a Kelvin–Helmholtz instability.

Considering the variety of phenomena which were identified during this investigation, the very simple configuration consisting of a sphere settling through a two-layer system of immiscible viscous fluids appears as a generic ‘device’ capable of providing a body of fundamental insight into several classes of apparently unrelated fluid dynamics problems. One of them is obviously the dynamics of objects of any sort moving across an interface in the presence of surface tension, viscosity contrast and buoyancy effects. This ranges from small, light objects close to flotation conditions, for which the dynamics of the meniscus plays a key role, to bodies with a large inertia for which the central issue is to determine the evolution of the tail volume, as it has a direct impact on the effective drag. Another class of problems where this ‘device’ may be helpful is the dynamics of stretched fluid filaments. In that context, it may be seen to some extent as a surrogate for the Taylor four-roll mill apparatus, since it allows the evolution of such ligaments to be studied under a broad variety of conditions. These include highly inertial situations which may result in tail fragmentation. Hence, by properly selecting the fluids and sphere properties, this system may also be used as a simple and well manageable substitute to the usual open-flow configurations, such as two-phase coaxial jets or mixing layers, to study fundamental mechanisms involved in the initiation of the fragmentation process.

The present paper only considered axisymmetric configurations, so that the transition to three-dimensional wake and tail dynamics was not examined. The non-axisymmetric tail geometries reported in figure 4 of PM1 suggest that the two dynamics are closely coupled. However we have no clue for the time being to figure out how the presence of a sharp interface involving a (possibly) large viscosity jump, not mentioning effects of density contrast and interfacial tension, alters the established transition scenario for the wake past a sphere in a homogeneous fluid. We believe that this is an original aspect of the present class of flows deserving future consideration.

Last, the modelling of the various contributions to the hydrodynamic force experienced by the sphere was not addressed here, although it clearly represents a major objective in terms of applications. The static limit corresponding to the sphere floating at the interface is reasonably well understood, although rigorous

predictions are available only in the limit where capillary effects are large compared to buoyancy effects induced by the fluid density contrast (see §4 of PM1). Some attempts have also been reported in the literature to account for the influence of the entrained fluid in the context of linearly stratified flows or miscible fluids under specific conditions, especially in the inviscid and Stokes flow limits. The key issue for future studies is of course to derive tractable models capable of predicting how the geometry, hence the volume, of the entrained tail evolves, both with miscible and immiscible fluids, under a broad range of conditions. Such models should also include a prediction of the pinch-off location, as it determines how much fluid remains stuck to the sphere. Significant progress was recently achieved in that direction in the case of a sphere impacting a free surface. However, in liquid–liquid configurations, fluid inertia within the tail requires more sophisticated approaches. This is why deriving a rational modelling approach encompassing all main phenomena influencing the sphere motion and capable of dealing (through semi-empirical extensions) with situations in which inertia and viscosity of both fluids interplay remains a real challenge.

Acknowledgements

Computations performed with JADIM owe much to the continuous support of A. Pédrone and to the expertise of F. Auguste with the VOF approach; we also acknowledge fruitful discussions with T. Bonometti and Y. Hallez about the IBM technique and with F. Charru about shear instabilities. J.-L.P.’s fellowship was provided by the Délégation Générale de l’Armement whose financial support is greatly appreciated. This work was granted access to the HPC resources of CALMIP under allocation 2013-P13132.

Appendix A. Technical aspects of the immersed boundary technique

Preliminary tests carried out with the version of the IBM technique described by Bigot *et al.* (2014) revealed some limitations or inaccuracies. Therefore we introduced several modifications which significantly improve the quality of the numerical predictions and the range of applicability of this technique in the framework of the JADIM code. A detailed presentation of these changes may be found in Pierson (2015) and we only summarize them below.

First, we modified the distribution of the volume fraction α involved in (2.6) to avoid an excessive spreading of the forcing over pure fluid regions, while maintaining a smooth variation across the sphere surface $\|\mathbf{r}\| = R$ to prevent the occurrence of spurious oscillations of the fluid–solid coupling. For this purpose, we followed the suggestion of Nakayama & Yamamoto (2005) and imposed a sine distribution of α within a spherical shell $R - \Delta \leq \|\mathbf{r}\| \leq R + \Delta$ so as to smoothly match with the uniform distributions $\alpha = 1$ (respectively 0) in the regions $\|\mathbf{r}\| < R - \Delta$ (respectively $\|\mathbf{r}\| > R + \Delta$). Extensive tests showed that the best choice for Δ is $\Delta = (3/2)\Delta x$, where Δx stands for the cell size.

A second improvement dealt with the way the prescribed velocity \mathbf{U}_D is defined in the fluid part of the transition region corresponding to $0 < \alpha < 1/2$. Various tests revealed that imposing $\mathbf{U}_D = \mathbf{V}$ in that region tends to overestimate boundary layer effects (hence the drag on the body) because it constrains the fluid to move with the body velocity within the peripheral shell $R \leq \|\mathbf{r}\| \leq R + \Delta$. To reduce this effect and better account for the influence of the surrounding fluid, we impose $\mathbf{U}_D = \alpha \mathbf{V} + (1 - \alpha)\mathbf{U}_I$, where \mathbf{U}_I is a local fluid velocity resulting from a multidirectional linear

interpolation of \mathbf{U} over the neighbouring cells, along the scheme proposed by Ikeno & Kajishima (2007).

We also implemented an important improvement due to Kempe & Fröhlich (2012) within each substep of the third-order Runge–Kutta/Crank–Nicolson advancement scheme. This change removes the well-known limitation experienced with Uhlmann’s (2005) technique when dealing with ‘light’ bodies, i.e. those for which ρ_p/ρ is of $O(1)$ or less. Indeed, replacing $\int_S \boldsymbol{\Sigma} \cdot \mathbf{n} dS$ by $\rho(d\mathbf{V}/dt - \mathbf{g})\mathcal{V} - \int_V \mathbf{F}_{IBM} dV$ as proposed by Uhlmann (2005), one readily finds that (2.7) yields $d\mathbf{V}/dt = \mathbf{g} - \{(\rho_p - \rho)\mathcal{V}\}^{-1} \int_V \mathbf{F}_{IBM} dV$, which obviously diverges when the density difference $\rho_p - \rho$ tends toward zero. Kempe & Fröhlich (2012) pointed out that the origin of the problem stems from the fact that Uhlmann’s surrogate for $\int_S \boldsymbol{\Sigma} \cdot \mathbf{n} dS$, in which the material derivative $d/dt \int_V \rho \mathbf{U} dV$ is transformed into $\rho \mathcal{V} d\mathbf{V}/dt$, requires the fluid velocity field \mathbf{U} within \mathcal{V} to correspond to a rigid-body motion, which may not be strictly the case in the course of the iterations. Removing this assumption, equation (2.7) yields the body acceleration in the more general form $d\mathbf{V}/dt = (1 - \rho/\rho_p)\mathbf{g} + \{\rho_p \mathcal{V}\}^{-1} \{d/dt \int_V \rho \mathbf{U} dV - \int_V \mathbf{F}_{IBM} dV\}$ which removes the divergence. As suggested by Kempe & Fröhlich (2012), we evaluate the time derivative of the fluid momentum $\int_V \rho \mathbf{U} dV$ within each substep of the Runge–Kutta algorithm using a forward Euler scheme.

The last modification we introduced is intended to reduce the inconsistency usually experienced when an explicit treatment of the forcing term \mathbf{F}_{IBM} is combined with an implicit (or partly implicit) time advancement of the Navier–Stokes equation. In the present case, the Crank–Nicolson algorithm used to advance the viscous term in (2.4) requires the solution of an unsteady Stokes equation, and the corresponding increment in the fluid velocity, say $\delta \mathbf{U}$, may be shown to be proportional to $\nu \Delta t^2$. Usually, the forcing (2.6) is evaluated explicitly at the end of each Runge–Kutta substep, prior to the corresponding Crank–Nicolson step. Hence after the latter, the fluid and body velocities within the body volume \mathcal{V} differ from each other by $\delta \mathbf{U}$, and the smaller the Reynolds number the larger this difference. Kempe & Fröhlich (2012) showed that this issue may be fixed, i.e. the no-slip condition may be properly enforced, by creating a forcing loop. We adapted their suggestion by introducing a loop on the entire forcing/Crank–Nicolson step, using the fluid velocity resulting from the solution of the unsteady Stokes equation at iteration $n - 1$ to evaluate the force \mathbf{F}_{IBM} at iteration n and involving the latter in the right-hand side of the unsteady Stokes equation at the next iteration. In practice, we found that two iterations of this sequential process suffice to obtain negligible slip velocities $\mathbf{U} - \mathbf{V}$ within the body at the end of a complete Runge–Kutta/Crank–Nicolson step.

Figure 19 shows how the modified method incorporating the above four changes works for $O(1)$ solid-to-fluid density ratios in the case of a single sphere sedimenting in the low-to-moderate Reynolds number regime. The reference experiments are those of Ten Cate *et al.* (2002); raw data files were kindly provided by Dr Ten Cate. Only 20 cells are distributed over one sphere radius (to compare with the predictions of Kempe & Fröhlich 2012) but the results show that the evolution of the settling velocity is faithfully captured in all four cases during the (negative) acceleration time period and the ‘plateau’ which follows. During the final stage, a slight shift increasing as the Reynolds number decreases may be noticed. It merely results from the slight overestimate of the settling velocity which exists throughout the descent, a result of the coarse resolution which does not entirely capture the velocity gradients close to the sphere and hence somewhat underestimates its drag. This effect accumulates over longer times in the low-Reynolds-number regime, making the sphere reach the neighbourhood of the lower wall somewhat too early.

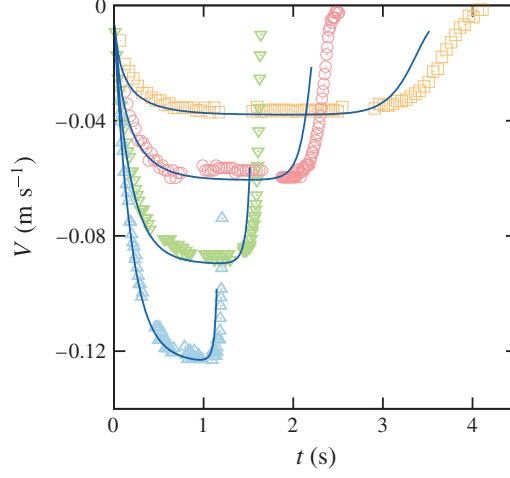


FIGURE 19. (Colour online) Comparison of computational predictions (solid lines) and experiments (symbols) from Ten Cate *et al.* (2002) for the settling velocity of a sphere sedimenting in a homogeneous fluid. The height and radius of the computational domain are $21.3R$ and $6.7R$, respectively, just as the experimental tank, and the sphere is released from rest $4.3R$ from the top surface. On the four curves, from top to bottom, the solid-to-fluid density ratio and the particle Reynolds number based on the particle radius and sedimentation velocity in an unbounded medium are $(1.155, 0.75)$, $(1.160, 2.05)$, $(1.164, 15.8)$ and $(1.167, 15.95)$, respectively.

Appendix B. Numerical solution of the Young–Laplace problem

To obtain an accurate description of the meniscus under quasi-static conditions, one generally has to resort to a numerical solution of the Young–Laplace equation $(\rho_2 - \rho_1)gz = \gamma \nabla \cdot \mathbf{n}(z)$, where \mathbf{n} is the outer unit normal to the meniscus surface. Setting $r^* = r/R$ and $z^* = z/R$ (where r stands for the radial distance to the symmetry axis) and considering that this surface is defined by the equation $r^* = \eta(z^*)$, the radial and axial components of \mathbf{n} are $1/(1 + \eta'^2)^{1/2}$ and $-\eta'/(1 + \eta'^2)^{1/2}$, respectively, the prime denoting differentiation with respect to z^* . Hence one has to solve

$$Boz^* = \frac{1}{\eta} \frac{1}{(1 + \eta'^2)^{1/2}} - \frac{\eta''}{(1 + \eta'^2)^{3/2}}. \quad (\text{B } 1)$$

Introducing the cap angle ψ such that $\psi = 0$ at the bottom of the sphere, the meniscus joins the sphere at a vertical position $z^* = z_s^*$ and a radial position $\eta = \sin \psi$ with a slope $\eta' = \cot \psi$, assuming total wetting (see figure 6 in PM1). It connects tangentially to the horizontal interface when $z^* \rightarrow 0$. Hence the whole set of boundary conditions reads

$$\left. \begin{aligned} \eta(z_s^*) &= \sin \psi, \\ \eta'(z_s^*) &= \cot \psi, \\ \eta(z^*) &\rightarrow +\infty \quad \text{for } z^* \rightarrow 0, \\ \eta'(z^*) &\rightarrow +\infty \quad \text{for } z^* \rightarrow 0. \end{aligned} \right\} \quad (\text{B } 2)$$

Following Huh & Scriven (1969) and Rapacchietta & Neumann (1977), we solve this problem using a shooting method combined with a fourth-order Runge–Kutta

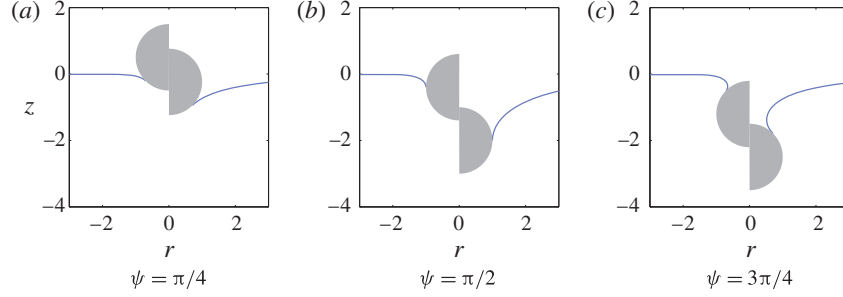


FIGURE 20. (Colour online) Meniscus profile for three different cap angles and two different Bond numbers. In each image, the left and right halves correspond to $Bo = 10$ and $Bo = 0.1$, respectively.

integration scheme for (B 1). To this end, we first assume z_s^* to be given by the approximate high- Bo model discussed in PM1 (see also Maru *et al.* 1971; Bonhomme *et al.* 2012), i.e. $z_s^* = \{1 - \sqrt{1 + 4Bo(1 - \cos \psi)}\}/2Bo$, enforce the two boundary conditions at the sphere surface and iterate the solution until the two boundary conditions at infinity are satisfied.

The shape of the meniscus obtained through this procedure is plotted in figure 20 for three different cap angles and two Bond numbers. The crucial influence of Bo may be appreciated in each image: the interface always deforms over a distance of the order of the capillary length $l_c = \sqrt{\gamma/((\rho_2 - \rho_1)g)}$, i.e. $l_c/R = Bo^{-1/2}$. Hence this deformation is limited to a small zone around the contact line when $Bo \gg 1$, whereas it extends over a wide region whose radius is much larger than the sphere radius in the opposite limit.

Appendix C. Influence of buoyancy on the retraction of a fluid thread

In this appendix we revisit the problem of the retraction of a thin column of viscous fluid surrounded by another, much less viscous fluid. We are primarily interested in reasons which can make the retraction velocity different from the classical Taylor–Culick prediction (Taylor 1959; Culick 1960), especially in the possible influence of buoyancy effects.

To begin with, we recall the equations governing the flow within the column, assuming an axisymmetric (r, z) geometry (with, throughout this appendix, the z axis pointing upwards) and considering the slender-body (or long-wave) limit $\epsilon = \mathcal{R}/\mathcal{L} \ll 1$, where $\mathcal{L}(t)$ denotes the length of the column and $\mathcal{R}(z, t)$ its local radius. Expanding the streamwise momentum balance in powers of ϵ , it is readily found that the streamwise velocity, $u_z(r, z, t)$, results from the linear superposition of a leading-order plug profile, $W(z, t)$, and a second-order Poiseuille-like contribution, $A(z, t)r^2$. Mass conservation also implies that, at leading order, the radial velocity, $u_r(r, z, t)$, obeys $u_r = -(r/2)W_z$, where the subscript stands for the partial derivative. The shear-free condition at the column surface may then be expressed in terms of derivatives of W only, and is satisfied by selecting $A = (3/2)(\mathcal{R}_z/\mathcal{R})W_z + (1/4)W_{zz}$. Finally, at order ϵ^0 , the radial momentum balance implies that the leading-order pressure, P , does not depend on the radial position. Hence, neglecting viscous and dynamic effects in the outer fluid, the normal stress balance at the column surface yields $P(z, t) = -\rho_2 g z + \gamma \nabla \cdot \mathbf{n} - \mu_1 W_z$, where \mathbf{n} denotes the outer unit normal to

the surface $r = \mathcal{R}(z, t)$. Combining these results, the mass and streamwise momentum balances are found to read, respectively,

$$\mathcal{R}_t + W\mathcal{R}_z = -\frac{1}{2}W_z\mathcal{R}, \quad (\text{C } 1)$$

$$\rho_1(W_t + WW_z) = (\rho_2 - \rho_1)g - \gamma(\nabla \cdot \mathbf{n})_z + 3\frac{\mu_1}{\mathcal{R}^2}(\mathcal{R}^2 W_z)_z. \quad (\text{C } 2)$$

These equations are identical to those obtained by Eggers & Dupont (1994), with the exception of the $\rho_2 g$ contribution since these authors neglected any influence of the surrounding medium. Multiplying (C 1) by $2\mathcal{R}W$, (C 2) by \mathcal{R}^2 , introducing the explicit expression of the mean curvature as given in (B 1) and rearranging yields the conservation equation for the momentum density $\rho_1 \mathcal{R}^2 W$ in the form

$$(\rho_1 \mathcal{R}^2 W)_t + \left\{ \rho_1 W^2 \mathcal{R}^2 - 3\mu_1 \mathcal{R}^2 W_z - \gamma \left[\frac{\mathcal{R}}{(1 + \mathcal{R}_z^2)^{1/2}} + \frac{\mathcal{R}^2 \mathcal{R}_{zz}}{(1 + \mathcal{R}_z^2)^{3/2}} \right] \right\}_z = (\rho_2 - \rho_1)g\mathcal{R}^2. \quad (\text{C } 3)$$

Assuming that the column extends from $z = 0$ to $z = -\mathcal{L}(t)$, its volume and total momentum are $\mathcal{V}_c = \pi \int_{-\mathcal{L}(t)}^0 \mathcal{R}^2 dz$ and $\mathcal{P}_c = \pi \int_{-\mathcal{L}(t)}^0 \rho_1 \mathcal{R}^2 W dz$, respectively. Then, noting that \mathcal{R} vanishes at the tip, i.e. $\mathcal{R}(z = -\mathcal{L}(t)) = 0 \forall t$, integration of (C 1) (once multiplied by $2\mathcal{R}$) and (C 3) yields, respectively,

$$\frac{d\mathcal{V}_c}{dt} = -\pi \rho_1 W \mathcal{R}^2|_{z=0}, \quad (\text{C } 4)$$

$$\begin{aligned} \frac{d\mathcal{P}_c}{dt} = & (\rho_2 - \rho_1)g\mathcal{V}_c - \pi \rho_1 W^2 \mathcal{R}^2|_{z=0} + 3\pi \mu_1 \mathcal{R}^2 W_z|_{z=0} \\ & + \pi \gamma \left[\frac{\mathcal{R}}{(1 + \mathcal{R}_z^2)^{1/2}} + \frac{\mathcal{R}^2 \mathcal{R}_{zz}}{(1 + \mathcal{R}_z^2)^{3/2}} \right]_{z=0}. \end{aligned} \quad (\text{C } 5)$$

Provided that (i) the density contrast between the two fluids is negligible (or the column is horizontal), (ii) the fluid is at rest at $z = 0$, i.e. $W|_{z=0} = W_z|_{z=0} = 0$, and (iii) the radius of the column does not change in the vicinity of $z = 0$, i.e. $\mathcal{R}_z|_{z=0} = \mathcal{R}_{zz}|_{z=0} = 0$, equation (C 5) reduces to

$$\frac{d\mathcal{P}_c}{dt} = \pi \gamma \mathcal{R}|_{z=0}. \quad (\text{C } 6)$$

The classical reasoning (Taylor 1959; Culick 1960; Keller 1983; Keller, King & Ting 1995; Savva & Bush 2009) assumes that (iv) the full mass of fluid set in motion by the retraction process feeds a spherical blob (or a circular rim in the two-dimensional case) at the tip, while the fluid located in between the blob and the basis of the column or sheet stays at rest. The velocity at which the blob recedes is $-d\mathcal{L}/dt$ and the mass flowrate entering it is $-\pi \rho_1 \mathcal{R}_B^2 d\mathcal{L}/dt$, where \mathcal{R}_B stands for the radius just past the blob. Hence, after the initial transient during with $d^2\mathcal{L}/dt^2 \neq 0$, the momentum rate of change reduces to $d\mathcal{P}_c/dt = \pi \rho_1 \mathcal{R}_B^2 (d\mathcal{L}/dt)^2$. With the final assumption that (v) the radius does not vary from the position of the blob to $z = 0$, i.e. $\mathcal{R}|_{z=0} = \mathcal{R}_B$, one obtains the Taylor–Culick velocity $W_{TC} = -d\mathcal{L}/dt$, namely

$$W_{TC} = \sqrt{\frac{\gamma}{\rho_1 \mathcal{R}_B}}. \quad (\text{C } 7)$$

This result differs from the one originally obtained by Keller (1983) by a factor of $\sqrt{2}$ but agrees with that of Hoepffner & Paré (2013). Both groups performed an inviscid momentum balance over the entire blob, but Keller omitted to take into account the capillary contribution γ/\mathcal{R}_B within the cylindrical part of the column. The latter reduces the pressure difference with the blob interior by a factor of two, which is why the correct result is (C 7). Although the schematic view corresponding to assumption (iv) is valid in most cases, Brenner & Gueyffier (1999) showed that it does not apply when the Reynolds number of the column, $Re_{\mathcal{L}} = \rho_1 V_{TC} \mathcal{L} / \mu_1$, is small (strictly speaking $\ll 1$), in which case no rim or blob forms at the tip and the column merely thickens uniformly as it recedes.

The situation considered in § 5.1 is far from satisfying the whole set of conditions (i)–(v). In particular, the column broadens dramatically at its top, making (iii) and (v) unrealistic. Moreover, the ratio of the first and last terms in the right-hand side of (C 5) is of $O((\rho_2 - \rho_1)g\mathcal{R}\mathcal{L}/\gamma) = O(Bo\mathcal{R}\mathcal{L}/R^2)$. According to figure 14(a,b), the top region within which \mathcal{R} strongly varies with the vertical position extends approximately over 5 sphere radii. Hence, the initial length \mathcal{L}_0 of the remaining part of the column, on which the rest of this analysis focuses, is typically 10–15 R . Its average radius, \mathcal{R}_m , may be estimated from figure 14(c,d), which yields $\mathcal{R}_m \approx 0.3R$ – $0.4R$. Since $Bo = 0.24$, these estimates indicate that $0.7 \lesssim Bo\mathcal{R}_m\mathcal{L}_0/R^2 \lesssim 1.4$. Hence, buoyancy and capillary contributions are of the same order of magnitude, so that assumption (i) is not satisfied. In contrast, (ii) (with now $z = -5R$ instead of $z = 0$) looks reasonable as far as the column remains long enough for the flow rate through its base to remain small. Finally, setting $\mathcal{R}_B = \mathcal{R}_m$ in (C 7) and $\mathcal{L} = \mathcal{L}_0$ in the definition of $Re_{\mathcal{L}}$, the column Reynolds number is found to be in the range 10–20. Hence assumption (iv) is satisfied, as confirmed by figure 14(c–f) in which a blob is clearly present.

Based on the above estimates, the simplest model which can reasonably hold in the present situation is that of a cylindrical column of radius \mathcal{R}_m and initial length \mathcal{L}_0 in which the retraction dynamics obey the approximate form of (C 5)

$$\frac{d\mathcal{P}_{cm}}{dt} = (\rho_2 - \rho_1)g\mathcal{V}_{cm} + \pi\gamma\mathcal{R}_m, \quad (\text{C } 8)$$

with $\mathcal{V}_{cm} = \pi\mathcal{R}_m^2\mathcal{L}$ and $d\mathcal{P}_{cm}/dt = \pi\rho_1\mathcal{R}_m^2(d\mathcal{L}/dt)^2$. This model yields the differential equation

$$\left(\frac{d\mathcal{L}}{dt}\right)^2 = \zeta g\mathcal{L} + \frac{\gamma}{\rho_1\mathcal{R}_m} \quad \text{with } \mathcal{L}(t=0) = \mathcal{L}_0, \quad (\text{C } 9)$$

the solution of which provides the buoyancy-modified Taylor–Culick velocity $W_{TCg} = -d\mathcal{L}/dt$ as

$$W_{TCg} = \sqrt{\zeta g\mathcal{L}_0 + \frac{\gamma}{\rho_1\mathcal{R}_m}} - \frac{1}{2}\zeta gt. \quad (\text{C } 10)$$

The shortening of the column makes W_{TCg} decrease linearly over time. However, for short enough times, i.e. $t \ll \sqrt{\mathcal{L}_0/(\zeta g)} + \gamma/(\zeta^2\rho_1\mathcal{R}_mg^2)$, the model still predicts a virtually constant velocity which is larger than the classical Taylor–Culick prediction, W_{TC} , owing to the cooperative effect of buoyancy. Using the above estimates for the situation of § 5.1, equation (C 10) yields $1.4 \lesssim W_{TCg}/W_{TC} \lesssim 1.5$, so that buoyancy is found to increase the purely capillary-driven retraction velocity by 40%–50%.

Appendix D. Interfacial instability past high-inertia spheres sinking in a low-viscosity fluid

In this appendix we investigate the possible instability scenarios which may explain the initiation of the corollas observed in the wake of high-inertia spheres settling in a weakly viscous fluid. According to the second panel in figure 18, the wavelength of the disturbance which develops along the sphere is approximately $0.6R$, corresponding to a wavenumber $k \approx 10.5R^{-1}$, and the thickness h of the film surrounding the sphere in that region is $0.2\text{--}0.3R$. This wavelength being approximately one-tenth the sphere circumference (also one-tenth the circumference of the column whose radius is of $O(R)$ close to the sphere), it is enough to consider the problem in a plane. We also note that $kh \approx 2.1\text{--}3.2$, which suggests that finite-depth effects within the film are small since $1.004 \leq \coth kh \leq 1.03$. A first candidate to explain the growth of the observed disturbance could be the Rayleigh–Taylor instability, since the heavier fluid stands on top of the lighter one in some parts of this region. Nevertheless, the capillary length $l_c = RBo^{-1/2}$ being approximately $1.5R$ since the density contrast is small, kl_c is about 16, which is well beyond the cutoff wavenumber $k_{co} = l_c^{-1}$ (Chandrasekar 1961). This clearly rules out this possibility and makes shear-induced instabilities, be they viscous or inviscid by nature, the most plausible explanation.

To explore this second possibility, we first need an estimate of the shear stress on both sides of the interface, keeping in mind that the outer fluid is at rest far from the column but its central region is entrained downwards, owing to the matching of the shear stresses at the interface (see figure 21). To determine the thickness $\delta_2(z)$ of the corresponding boundary layer at a local position z , a crude reasoning consists in assuming that the entire column goes down with the (now dimensional) sphere velocity V and entrains a layer of outer fluid whose local thickness is approximately $\sqrt{\pi\mu_2 t / \rho_2}$, where t denotes the time a material particle standing at position z on the column surface has been in contact with the lower fluid after the sphere has crossed the initial flat interface. This estimate is directly inspired by Stokes’ first problem where a fluid layer is set in motion by the impulsive start of a plate which then moves with a constant velocity (with this definition of δ_2 , the velocity falls to zero at the edge of the boundary layer, assuming a uniform shear rate V/δ_2 throughout it). Thus, on the sphere equator, $t = \int_0^L V^{-1}(z_0) dz_0$ when the sphere centre stands at a depth L from the initial interface position. Provided that V has varied in a quasi-steady manner since $z_0 = 0$, one then has $\delta_2(L) \approx (\pi\mu_2/\rho_2 \int_0^L V^{-1}(z_0) dz_0)^{1/2}$, which yields $\Delta_2 = \delta_2(L)/R \approx 0.06$ when $L/R \approx 5$ which corresponds to the second panel of figure 18; this estimate is qualitatively consistent with the thickness of the interfacial vortical layers in figure 16(*h,i*). The shear rate within the boundary layer being V/δ_2 , the matching of viscous stresses at the column surface implies that, in the bottom part of the column, the shear rate G_1 at the interface is $\lambda V/\delta_2(L)$, which allows us to define the viscous length scale $l_{\mu_1} = (\mu_1/(\rho_1 G_1))^{1/2}$, i.e. $l_{\mu_1}/R \approx 1.6$ still when $L/R \approx 5$. This viscous length being of $O(R)$, the flow within the column is influenced up to the axis by the interfacial shear stress (in particular, the quadratic contribution $A(z)r^2$ to the vertical velocity $u_z(r, z, t)$ described in appendix C comprises an additional term $-2\lambda V(t)(\mathcal{R}(z)\delta_2(z))^{-1}r^2$). Around the sphere itself, the outer fluid is accelerated from the front pole to the equator (which is why the initial bump occurs close to the latter), making the velocity difference ΔU between the film and the outer fluid just outside the boundary layer be $3V/2$ on the equator instead of V along the column, as shown in figure 21. As far as the boundary layer around the sphere is growing due to diffusion, its thickness remains close to $\delta_2(L)$ down to the equator, which implies

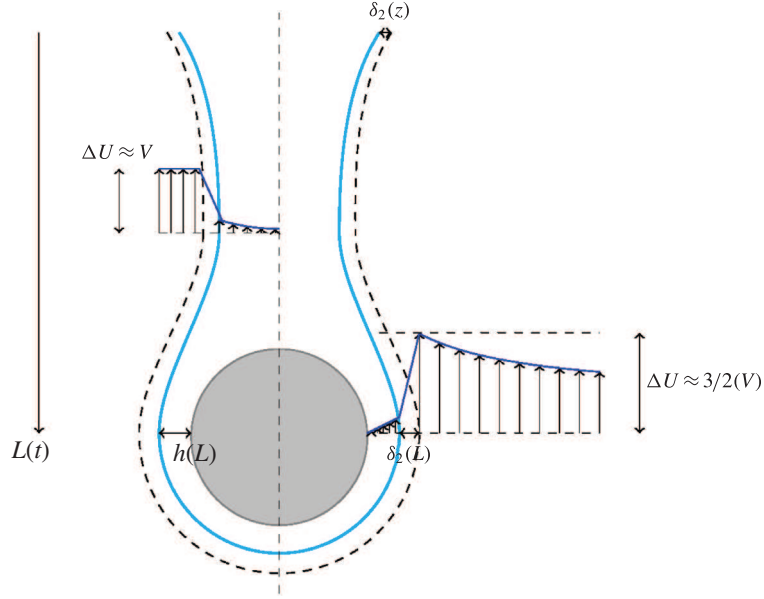


FIGURE 21. (Colour online) Sketch of the flow past the sphere and the bottom part of the tail in a reference frame translating with the sphere.

that the shear rate is approximately increased to $(3/2)V/\delta_2(L)$ there. Having estimated $\delta_2(L)$, l_{μ_1} and ΔU , we can now examine the two families of shear instabilities which can develop at the interface in the vicinity of the sphere.

The first of them is of course the Kelvin–Helmholtz instability. The radial velocity gradient in the potential flow past the sphere is of $O(V/R)$ and the shear within the film is of $O(G_1)$, both of which are small compared to $V/\delta_2(L)$. Hence, as a first approximation, the flow near the sphere equator may be considered as made of two uniform streams with a velocity difference $\Delta U = (3/2)V$, separated by a uniform shear layer with a thickness $\delta_U = \delta_2(L)$, which allows us to make use of classical predictions established for a piecewise linear velocity profile (Rayleigh 1879; Chandrasekar 1961). In such a case, neglecting surface tension, the wavenumber k_{KH} of the most amplified disturbance is known to satisfy $k_{KH}\delta_U \approx 0.8$, which here yields $k_{KH}R \approx 13.7$; the corresponding growth rate β_{KH} is $0.2\Delta U/\delta_U$, i.e. $0.3\lambda^{-1}G_1 = 150G_1$. These classical results may be readily modified to include surface tension effects in the corresponding dispersion relation (see e.g. Marmottant & Villermaux 2004b). Defining the Weber number $We_T = \rho_1\delta_U(\Delta U)^2/\gamma$ and assuming $\rho_2 = \rho_1$, it may be shown that for large We_T , the most amplified wavenumber and the associated growth rate become, respectively,

$$k_{KH}\delta_U \approx 0.8(1 - 4.0We_T^{-1}) \quad \text{and} \quad \beta_{KH} \frac{\delta_U}{\Delta U} \approx 0.2(1 - 3.2We_T^{-1}). \quad (\text{D } 1a,b)$$

These approximations are in excellent agreement with the results of the complete numerical calculations reported by Alabduljalil & Rangel (2006). Here $We_T \approx 19.7$, so that (D 1) yields $k_{KH}R \approx 10.9$ and $\beta_{KH}/G_1 \approx 125$, respectively. Although the very small difference ($<5\%$) between the predicted k_{KH} and the measured wavenumber k should not be taken too seriously, given the uncertainty on δ_2 and the non-parallel character of

the base flow, the fact that $k_{KH}/k = O(1)$ suggests that the Kelvin–Helmholtz instability is a plausible candidate to explain the evolution observed in figure 18.

This view is reinforced by the fact that (D 1) also explains why no instability is observed in the situation considered in § 5.1, although a bulge is clearly present in figure 12(e,k) near the sphere equator. In that case, the sphere velocity is almost three times smaller than in the previous configuration, owing to the much smaller sphere inertia and slightly smaller radius. In figure 12(e,k), $L/R \approx 9.5$, so that $V/(\zeta_p g R)^{1/2} \approx 1.1$ according to figure 13(a), which implies $\Delta_2 \approx 0.19$. As may be noticed in panel (k), this value of Δ_2 is consistent with the thickness of the vortical layer near the bottom of the column. Since $\Delta U = V$ there, one has $We_T \approx 2.5$, which yields $\beta_{TH} \approx -30G_1$ according to the second of (D 1), predicting correctly that the disturbance is damped in that region. Near the sphere equator, the boundary layer is seen to be much thinner than the above value of Δ_2 , in contrast to our previous assumption. This is because it stopped growing earlier, the balance between advection and radial diffusion of vorticity about the sphere having already been achieved. Clearly, the actual Δ_2 is 2–3 times smaller than the above estimate in that second region. Hence, despite the increase of ΔU to $3V/2$, We_T stays approximately in the range 1.9–2.8, keeping the local growth rate negative according to (D 1).

A second type of shear instability is known to exist under certain conditions in the presence of a viscosity stratification. It has been extensively studied since Yih’s pioneering investigation (Yih 1967); a comprehensive classification of the corresponding instabilities was given by Charru & Hinch (2000) and a review of the field was recently provided by Govindarajan & Sahu (2014). In a bounded two-layer Couette configuration with each layer characterized by a thickness h_i and a shear rate G_i ($i = 1, 2$), the behaviour of such instabilities crucially depends on the length scale ratios kh_i and kl_{μ_i} , with $l_{\mu_i} = (\mu_i/(\rho_i G_i))^{1/2}$. Yih’s analysis corresponds to the long-wave limit $kh_i \ll 1$ and $kl_{\mu_i} \ll 1$, in which case it is found that the flow is unstable when the thinner layer is the more viscous. This qualitative result extends, although with a larger growth rate, to the semi-bounded case corresponding to $kh_2 \rightarrow \infty$ (Hooper 1985). The opposite short-wave limit, $kh_i \gg 1$ and $kl_{\mu_i} \gg 1$, was considered by Hooper & Boyd (1983) who showed that, provided $\lambda \neq 1$, the interface is always unstable to such perturbations (in the absence of surface tension). Wall effects were examined in the semi-bounded configuration by Hooper & Boyd (1987), especially with the intermediate combination $kl_{\mu_i} \ll 1$ and $h/l_{\mu_1} \gg 1$, where another unstable mode was identified when the bounded layer is the less viscous.

Although this is generally not stated explicitly, all these investigations actually assume that the viscosity ratio is ‘not too far’ from unity. This is apparent in the fact that kl_{μ_i} is assumed to be simultaneously small or large in both fluids, although the continuity of shear stresses merely implies $l_{\mu_2} = \lambda(1 + \zeta)^{1/2} l_{\mu_1}$. The disturbance observed experimentally here corresponds to $kl_{\mu_1} \approx 17$. However, since $\lambda = 2. \times 10^{-3}$, one has $kl_{\mu_2} \approx 0.035$, which shows that this disturbance is much shorter than the viscous scale in the more viscous fluid but much longer than its counterpart in the outer fluid. To the best of our knowledge, such a mixed situation has not been worked out theoretically, leaving us without any clear indication about the growth rate of the corresponding potentially unstable modes. In addition, one has to notice that $kh_1 \approx 2.5$ and $k\delta_2 \approx 0.6$, so that additional effects due to the finite thickness of both shear layers are expected; in particular, the $O(1)$ value of $k\delta_2$ suggests that the problem actually involves three layers rather than two, since the disturbance certainly interacts with the unbounded outer fluid as it does in the above simplified model of the Kelvin–Helmholtz instability. The only clue at hand to go one step

further is provided by the numerical investigations of Boeck & Zaleski (2005) and Otto *et al.* (2013) who solved the Orr–Sommerfeld problem for two-phase mixing layers characterized by error function or piecewise linear velocity profiles. Although they were mostly interested in gas–liquid configurations characterized by very small density ratios, i.e. $\zeta \rightarrow -1$, they also examined the influence of ζ for some specific viscosity ratios, identifying the nature of the dominant mode by comparing viscous and inviscid predictions. Their results (which correspond to high-Reynolds-number conditions, with Reynolds numbers based on the boundary layer thickness 3–30 times higher than in the present configuration) indicate that unstable modes due to viscosity stratification are indeed present but that the inviscid (Kelvin–Helmholtz) mode dominates as soon as the two fluid densities are close enough. More precisely, they found it to be dominant for $\zeta \geq -0.5$ when $\lambda = 10^{-1}$ and for $\zeta \geq -0.9$ when $\lambda = 10^{-2}$. Since $\lambda = 2 \times 10^{-3}$ and $\zeta = 0.03$ here, this is a strong indication that the Kelvin–Helmholtz mode also dominates under the present conditions.

It is of interest to notice that a horizontal sharp density stratification, such as that existing here due to the density jump between the tail and the outer fluid, may be responsible for a specific shear-induced, Reynolds-number-independent, long-wave instability, qualitatively similar to that analysed by Yih (1967). This instability was studied by Camassa *et al.* (2012), who considered, both theoretically and experimentally, a configuration in which a vertical infinite fibre is towed at a constant velocity in a two-layer fluid arrangement with uniform viscosity. Viscous entrainment then generates a column of heavy fluid around the fibre. Their theoretical analysis shows that, for large enough column radii, i.e. long enough times, the flow and column surface are unstable to long-wave disturbances. However, similar to instabilities due to viscous stratification, this instability exhibits very small growth rates, and for this reason could not be observed during the finite time of their experiments. This characteristic, combined with the fact that the viscosity contrast is much larger than the density contrast in the configurations considered here ($\lambda \approx 2 \times 10^{-3}$, $\zeta \approx 0.03$), makes it very unlikely that this instability may play a role under the present conditions.

REFERENCES

- ABAID, N., ADALSTEINSSON, D., AGYAPONG, A. & MCLAUGHLIN, R. M. 2004 An internal splash: Levitation of falling spheres in stratified fluids. *Phys. Fluids* **16**, 1567–1580.
- ALABDULJALIL, S. & RANGEL, R. H. 2006 Inviscid instability of an unbounded shear layer: effect of surface tension, density and velocity profile. *J. Engng Math.* **54**, 99–118.
- ARISTOFF, J. M. & BUSH, J. W. M. 2009 Water entry of small hydrophobic spheres. *J. Fluid Mech.* **619**, 45–78.
- BATCHELOR, G. K. 1967 *An Introduction to Fluid Dynamics*. Cambridge University Press.
- BIGOT, B., BONOMETTI, T., LACAZE, L. & THUAL, O. 2014 A simple immersed-boundary method for solid–fluid interaction in constant- and stratified-density flows. *Comput. Fluids* **97**, 126–142.
- BLANCHETTE, F. & SHAPIRO, A. M. 2012 Drops settling in sharp stratification with and without Marangoni effects. *Phys. Fluids* **24**, 042104.
- BOECK, T. & ZALESKI, S. 2005 Viscous versus inviscid instability of two-phase mixing layers with continuous velocity profile. *Phys. Fluids* **17**, 032106.
- BONHOMME, R., MAGNAUDET, J., DUVAL, F. & PIAR, B. 2012 Inertial dynamics of air bubbles crossing a horizontal fluid–fluid interface. *J. Fluid Mech.* **707**, 405–443.
- BONOMETTI, T. & MAGNAUDET, J. 2007 An interface-capturing method for incompressible two-phase flows: validation and application to bubble dynamics. *Intl J. Multiphase Flow* **33**, 109–133.

- BRACKBILL, J. U., KOTHE, D. B. & ZEMACH, C. 1992 A continuum method for modeling surface tension. *J. Comput. Phys.* **100**, 335–354.
- BRENNER, M. P. & GUEYFFIER, D. 1999 On the bursting of viscous films. *Phys. Fluids* **11**, 737–739.
- CALMET, I. & MAGNAUDET, J. 1997 Large-eddy simulation of high-Schmidt number mass transfer in a turbulent channel flow. *Phys. Fluids* **9**, 438–455.
- CAMASSA, R., KHATRI, S., MCLAUGHLIN, R. M., PRAIRIE, J. C., WHITE, B. L. & YU, S. 2013 Retention and entrainment effects: experiments and theory for porous spheres settling in sharply stratified fluids. *Phys. Fluids* **25**, 081701.
- CAMASSA, R., MCLAUGHLIN, R. M., MOORE, M. N. J. & YU, S. 2012 Stratified flows with vertical layering of density: experimental and theoretical study of flow configurations and their stability. *J. Fluid Mech.* **690**, 571–606.
- CHANDRASEKAR, S. 1961 *Hydrodynamic and Hydromagnetic Stability*. Oxford University Press.
- CHARRU, F. & HINCH, E. J. 2000 Phase diagram of interfacial instabilities in a two-layer Couette flow and mechanism of the long-wave instability. *J. Fluid Mech.* **414**, 195–223.
- COHEN, I., BRENNER, M. P., EGGERS, J. & NAGEL, S. R. 1998 Two fluid drop snap-off problem: experiments and theory. *Phys. Rev. Lett.* **83**, 1147–1150.
- CULICK, F. E. C. 1960 Comments on a ruptured soap film. *J. Appl. Phys.* **31**, 1128–1129.
- DIETRICH, N., PONCIN, S. & LI, H. Z. 2011 Dynamical deformation of a flat liquid–liquid interface. *Exp. Fluids* **50**, 1293–1303.
- EGGERS, J. 1993 Universal pinching of 3D axisymmetric free-surface flow. *Phys. Rev. Lett.* **71**, 3458–3460.
- EGGERS, J. & DUPONT, T. F. 1994 Drop formation in a one-dimensional approximation of the Navier–Stokes equation. *J. Fluid Mech.* **262**, 205–221.
- EGGERS, J. & FONTELOS, M. 2015 *Singularities: Formation, Structure, and Propagation*. Cambridge University Press.
- EGGERS, J. & VILLERMAUX, E. 2008 Physics of liquid jets. *Rep. Prog. Phys.* **71**, 036601.
- FABRE, D., TCHOUFAG, J. & MAGNAUDET, J. 2012 The steady oblique path of buoyancy-driven disks and spheres. *J. Fluid Mech.* **707**, 24–36.
- GELLER, A. S., LEE, S. H. & LEAL, L. G. 1986 The creeping motion of a spherical particle normal to a deformable interface. *J. Fluid Mech.* **169**, 27–69.
- GOVINDARAJAN, R. & SAHU, K. C. 2014 Instabilities in viscosity-stratified flow. *Annu. Rev. Fluid Mech.* **46**, 331–353.
- HARTLAND, S. 1968 The approach of a rigid sphere to a deformable liquid/liquid interface. *J. Colloid Interface Sci.* **26**, 383–394.
- HARTLAND, S. 1969 The profile of the draining film between a rigid sphere and a deformable fluid–liquid interface. *Chem. Engng Sci.* **24**, 987–995.
- HOEPFFNER, J. & PARÉ, G. 2013 Recoil of a liquid filament: escape from pinch-off through creation of a vortex ring. *J. Fluid Mech.* **734**, 183–197.
- HOOPER, A. P. 1985 Long-wave instability at the interface between two viscous fluids: thin layer effects. *Phys. Fluids* **28**, 1613–1618.
- HOOPER, A. P. & BOYD, W. G. C. 1983 Shear-flow instability at the interface between two viscous fluids. *J. Fluid Mech.* **128**, 507–528.
- HOOPER, A. P. & BOYD, W. G. C. 1987 Shear-flow instability due to a wall and a viscosity discontinuity at the interface. *J. Fluid Mech.* **179**, 201–225.
- HUH, C. & SCRIVEN, L. E. 1969 Shapes of axisymmetric fluid interfaces of unbounded extent. *J. Colloid Interface Sci.* **30**, 323–337.
- IKENO, T. & KAJISHIMA, T. 2007 Finite-difference immersed boundary method consistent with wall conditions for incompressible turbulent flow simulations. *J. Comput. Phys.* **226**, 1485–1508.
- JEFFREYS, G. V. & DAVIES, G. A. 1971 Coalescence of liquid droplets and liquid dispersion. In *Recent Advances in Liquid–Liquid Extraction* (ed. C. Hanson), chap. 14, pp. 495–584. Pergamon.
- JOHNSON, R. E. 1981 Stokes flow past a sphere coated with a thin fluid film. *J. Fluid Mech.* **110**, 217–238.

- JONES, A. F. & WILSON, S. D. R. 1978 The film drainage problem in droplet coalescence. *J. Fluid Mech.* **87**, 263–288.
- KELLER, J. B. 1983 Breaking of liquid films and threads. *Phys. Fluids* **26**, 3451–3453.
- KELLER, J. B., KING, A. & TING, L. 1995 Blob formation. *Phys. Fluids* **7**, 226–228.
- KEMIHA, M. 2006 Etude expérimentale des écoulements diphasiques: phénomènes interfaciaux. PhD thesis, Inst. Nat. Polytech. Lorraine, Nancy, France.
- KEMPE, T. & FRÖHLICH, J. 2012 An improved immersed boundary method with direct forcing for the simulation of particle laden flows. *J. Comput. Phys.* **231**, 3663–3684.
- LEE, S. H., CHADWICK, R. S. & LEAL, L. G. 1979 Motion of a sphere in the presence of a plane interface. Part 1. An approximate solution by generalization of the method of Lorentz. *J. Fluid Mech.* **93**, 705–726.
- LISTER, J. R. & STONE, H. A. 1998 Capillary breakup of a viscous thread surrounded by another viscous fluid. *Phys. Fluids* **10**, 2758–2764.
- MARMOTTANT, P. & VILLERMAUX, E. 2004a Fragmentation of stretched liquid ligaments. *Phys. Fluids* **16**, 2732–2741.
- MARMOTTANT, P. & VILLERMAUX, E. 2004b On spray formation. *J. Fluid Mech.* **498**, 73–111.
- MARU, H. C., WASAN, D. T. & KINTNER, R. C. 1971 Behavior of a rigid sphere at a liquid–liquid interface. *Chem. Engng Sci.* **26**, 1615–1628.
- MATAS, J. P. 2015 Inviscid versus viscous instability mechanism of an air–water mixing layer. *J. Fluid Mech.* **768**, 375–387.
- MIKAMI, T., COX, R. G. & MASON, S. G. 1975 Breakup of extending liquid threads. *Intl J. Multiphase Flow* **2**, 113–138.
- MITTAL, R. & IACCARINO, G. 2005 Immersed boundary methods. *Annu. Rev. Fluid Mech.* **37**, 239–261.
- NAKAYAMA, Y. & YAMAMOTO, R. 2005 Simulation method to resolve hydrodynamic interactions in colloidal dispersions. *Phys. Rev. E* **71**, 036707.
- O'BRIEN, S. B. G. 1996 The meniscus near a small sphere and its relationship to line pinning of contact lines. *J. Colloid Interface Sci.* **183**, 51–56.
- OTTO, T., ROSSI, M. & BOECK, T. 2013 Viscous instability of a sheared liquid–gas interface: dependence on fluid properties and basic velocity profile. *Phys. Fluids* **25**, 032103.
- PAPAGEORGIOU, D. T. 1995 On the breakup of viscous liquid threads. *Phys. Fluids* **7**, 1529–1544.
- PIERSON, J. L. 2015 Traversée d'une interface entre deux fluides par une sphère. PhD thesis, Inst. Nat. Polytech. Toulouse, Toulouse, France (available at <http://oatao.univ-toulouse.fr/15754/>).
- PIERSON, J. L. & MAGNAUDET, J. 2017 Inertial settling of a sphere through an interface. Part 1: from sphere flotation to wake fragmentation. *J. Fluid Mech.* **835**, 762–807.
- POWERS, T. R., ZHANG, D., GOLDSTEIN, R. E. & STONE, H. A. 1998 Propagation of a topological transition: the Rayleigh instability. *Phys. Fluids* **10**, 1052–1057.
- PROSPERETTI, A. & TRYGGVASON, G. 2007 *Computational Methods for Multiphase Flows*. Cambridge University Press.
- RAPACCHIETTA, A. V. & NEUMANN, A. W. 1977 Force and free-energy analyses of small particles at fluid interfaces. Part II. Spheres. *J. Colloid Interface Sci.* **59**, 555–567.
- RAYLEIGH, LORD 1878 On the instability of liquid jets. *Proc. Lond. Math. Soc.* **10**, 4–13.
- RAYLEIGH, LORD 1879 On the stability, or instability, of certain fluid motions. *Proc. Lond. Math. Soc.* **11**, 57–72.
- RIBE, N. M., HABIBI, M. & BONN, D. 2012 Liquid rope coiling. *Annu. Rev. Fluid Mech.* **44**, 249–266.
- SAVVA, N. & BUSH, J. W. M. 2009 Viscous sheet retraction. *J. Fluid Mech.* **626**, 211–240.
- SHOUKRY, E., HAFEZ, M. & HARTLAND, S. 1975 Separation of drops from wetted surfaces. *J. Colloid Interface Sci.* **53**, 261–270.
- SMITH, P. G. & VAN DE DEN, T. G. M. 1985 The separation of a liquid drop from a stationary solid sphere in a gravitational field. *J. Colloid Interface Sci.* **105**, 7–20.
- SMITH, P. G. & VAN DE VEN, T. G. M. 1984 The effect of gravity on the drainage of a thin liquid film between a solid sphere and a liquid/fluid interface. *J. Colloid Interface Sci.* **100**, 456–464.

- STONE, H. A. 1994 Dynamics of drop deformation and breakup in viscous fluids. *Annu. Rev. Fluid Mech.* **26**, 65–102.
- STONE, H. A., BENTLEY, B. J. & LEAL, L. G. 1986 An experimental study of transient effects in the breakup of viscous drops. *J. Fluid Mech.* **173**, 131–158.
- STONE, H. A. & LEAL, L. G. 1989 Relaxation and breakup of an initially extended drop in an otherwise quiescent fluid. *J. Fluid Mech.* **198**, 399–427.
- TAYLOR, G. 1959 The dynamics of thin sheets of fluid. Part III. Disintegration of fluid sheets. *Proc. R. Soc. Lond. A* **253**, 313–321.
- TEN CATE, A., NIEUWSTAD, C. H., DERKSEN, J. J. & VAN DEN AKKER, H. E. A. 2002 Particle imaging velocimetry experiments and lattice-Boltzmann simulations on a single sphere settling under gravity. *Phys. Fluids* **14**, 4012–4025.
- THOMPSON, M. C., LEWEKE, T. & HOURIGAN, K. 2007 Sphere–wall collisions: vortex dynamics and stability. *J. Fluid Mech.* **575**, 121–148.
- TJAHJADI, M., STONE, H. A. & OTTINO, J. M. 1992 Satellite and subsatellite formation in capillary breakup. *J. Fluid Mech.* **243**, 297–317.
- TOMOTIKA, S. 1935 On the instability of a cylindrical thread of a viscous liquid surrounded by another viscous fluid. *Proc. R. Soc. Lond. A* **150**, 322–337.
- UHLMANN, M. 2005 An immersed boundary method with direct forcing for the simulation of particulate flows. *J. Comput. Phys.* **209**, 448–476.
- YICK, K. Y., TORRES, C. R., PEACOCK, T. & STOCKER, R. 2009 Enhanced drag of a sphere settling in a stratified fluid at small Reynolds numbers. *J. Fluid Mech.* **632**, 49–68.
- YIH, C. S. 1967 Instability due to viscosity stratification. *J. Fluid Mech.* **27**, 337–352.
- YUKI, Y., TAKEUCHI, S. & KAJISHIMA, T. 2007 Efficient immersed boundary method for strong interaction problem of arbitrary shape object with the self-induced flow. *J. Fluid Sci. Technol.* **2**, 1–11.